THE ASTROPHYSICAL JOURNAL, 535:275–292, 2000 May 20
© 2000. The American Astronomical Society. All rights reserved. Printed in U.S.A.

2–45 MICRON INFRARED SPECTROSCOPY OF CARBON-RICH PROTO–PLANETARY NEBULAE[1]

BRUCE J. HRIVNAK
Department of Physics and Astronomy, Valparaiso University, Valparaiso, IN 46383; bruce.hrivnak@valpo.edu
AND
KEVIN VOLK AND SUN KWOK
Department of Physics and Astronomy, University of Calgary, Calgary, Alberta, Canada T2N 1N4; volk@iras.ucalgary.ca, kwok@iras.ucalgary.ca
Received 1999 July 6; accepted 2000 January 7

ABSTRACT

Infrared Space Observatory (*ISO*) 2–45 μm observations of seven proto–planetary nebulae (PPNs) and two other carbon-rich objects are presented. The unidentified emission features at 21 and 30 μm are detected in six sources, including four new detections of the 30 μm feature. This previously unresolved 30 μm feature is now resolved and found to consist of a broad feature peaking at 27.2 μm (the "30 μm" feature) and a narrower feature at 25.5 μm (the "26 μm" feature). This new 26 μm feature is detected in eight sources and is particularly strong in IRAS Z02229+6208 and 16594−4656. The unidentified infrared (UIR) emission features at 3.3, 6.2, 7.7, and 11.3 μm, which are commonly observed in planetary nebulae and H II regions, are also seen in these PPNs. However, their strengths relative to the continuum plateaus at 8 and 12 μm are weaker than in planetary nebulae. The 6.9 μm feature, seen almost exclusively in PPNs, is strong. New millimeter CO and HCN observations were made; they support the carbon-rich nature of the objects and yield the expansion velocities of the gaseous envelopes. The spectral energy distributions of these PPNs were fitted with a radiative-transfer model, taking into account the emission features at 21, 26, and 30 μm. A significant fraction of the total energy output is emitted in these features: as high as 20% in the 30 μm feature and 8% in the 21 μm feature. The fact that so much energy is carried in these features suggests that the material responsible for these features must be made of abundant elements and most likely involves carbon. SiS_2 appears to be ruled out as the emitter of the 21 μm feature due to the absence of a predicted companion feature.

Subject headings: circumstellar matter — infrared: ISM: lines and bands — planetary nebulae: general — radiative transfer — stars: AGB and post-AGB — infrared: stars

1. INTRODUCTION

The successful all-sky *Infrared Astronomical Satellite* (*IRAS*) returned photometric measurements of approximately 250,000 infrared sources around the sky during its 10 month lifetime in 1983. In addition to detecting the mid-infrared flux from the photospheres of normal stars, it also detected reemission from warm dust around many stars. Some of the latter are pre–main-sequence stars, some are main-sequence stars with Vega-like excesses, and many are asymptotic giant branch (AGB) stars, post-AGB stars, and planetary nebulae (PNs). Among the most important of the last of these is the detection of proto–planetary nebulae (PPNs), objects in transition between the AGB and the PN phases in the evolution of low- and intermediate-mass stars. Prior to the *IRAS* satellite, this transition phase was practically unexplored, but as a result of follow-up observations to the *IRAS* detections, several dozen good candidates are now known (Kwok 1993). Among the observational characteristics of a PPN is a double-peaked spectral energy distribution (SED), with flux in the visible and near-infrared coming from the reddened photosphere and flux in the mid- and far-infrared coming from the warm ($T \sim 150$–250 K) circumstellar dust.

The chemistry of circumstellar molecules and dust can be studied in the near- and mid-infrared. *IRAS* possessed a low-resolution spectrometer (LRS), which obtained 8–23 μm spectra of the brighter sources. These displayed the well-known silicate features in absorption and emission at 10 μm and in emission at 18 μm in oxygen-rich sources, and the silicon-carbide feature in emission at 11 μm in carbon-rich sources. These features are commonly seen in AGB and post-AGB stars. Also, the family of unidentified infrared (UIR) emission features generally ascribed to polycyclic aromatic hydrocarbon molecules (PAHs; Allamandola, Tielens, & Barker 1989) at 8.6 and 11.3 μm was seen in a number of carbon-rich sources, particularly PNs and PPNs. A new feature, first discovered in the *IRAS* LRS spectra, was a broad emission feature at $\sim$21 μm. This was first seen in four objects, all PPNs (Kwok, Volk, & Hrivnak 1989, hereafter KVH89) and has been detected in a total of 12 objects to date (Kwok, Volk, & Hrivnak 1999). All of the sources discovered so far with the "21 μm" feature appear to be carbon-rich PPNs (Hrivnak 1995). A very broad "30 μm" emission feature has also been detected in several AGB and PN sources (Forrest, Houck, & McCarthy 1981; Cox 1993). This 30 μm feature has also more recently been detected in five carbon-rich PPNs, all also possessing the 21 μm emission feature, through observations made with the Kuiper Airborne Observatory (KAO) by Omont et al. (1995, hereafter O95).

In the present study, the *Infrared Space Observatory* (*ISO*; Kessler et al. 1996) was used to observe the mid-infrared spectra of seven carbon-rich PPNs. Two additional cool *IRAS* sources were observed and found to display UIR features; they appear to be H II regions or young PNs and have been included for comparison. In Table 1 we list the

[1] Based on observations made with *ISO*, an ESA project with instruments funded by the ESA member states (especially the PI countries: France, Germany, the Netherlands, and the United Kingdom) with the participation of ISAS and NASA.

TABLE 1

SUMMARY OF GENERAL OBSERVATIONAL PROPERTIES OF PROGRAM OBJECTS

IRAS ID	V (mag)	Galactic Coordinates l(deg)	b(deg)	A_V [a] (mag)	Spectral Type	Visible Features	Millimeter Lines	V_{exp} (km s^{-1})	Reference
01005+7910.....	10.9	123.6	+16.6	0.8	OBe	...	...	...	1
02229+6208.....	12.1	133.7	+1.5	3.1	G8-K0 Ia	C_2, C_3, CN	CO, HCN	15	2, 3, 4
05341+0852.....	13.6	196.2	−12.1	1.2	G2 Ia	C_2, C_3, CN	CO, HCN	13	2, 3, 5
07134+1005.....	8.2	206.7	+10.0	0.6	F5 I	C_2, CN	CO, HCN	13	6, 7, 8, 9
18576+0341.....	>23	37.3	−0.2	2:	...	...	...	...	1
19306+1409.....	14.2	50.3	−2.5	2:	...	...	...	...	1
19477+2401.....	22.2	60.9	−1.0	3	...	...	CO	13	1, 3
20000+3239.....	13.3	69.7	+1.2	2.5	G8 Ia	C_2, CN	CO, HCN	12	7, 9, 10, 11
22574+6609.....	21.3	112.0	+6.0	3.2	...	...	CO, HCN	26	3, 12, 13

[a] Interstellar extinction derived from Neckel & Klare 1980 and Burnstein & Heiles 1982.

REFERENCES—References: (1) our unpublished observations; (2) Hrivnak & Kwok 1999; (3) this paper; (4) Reddy et al. 1999; (5) Reddy et al. 1997; (6) Hrivnak et al. 1989; (7) Hrivnak 1995; (8) Bakker et al. 1996; (9) Omont et al. 1993; (10) KHG95; (11) Bakker et al. 1997; (12) Hrivnak & Kwok 1991; (13) Su et al. 2000, in preparation.

program objects and some of their basic observational properties.

2. *ISO* SPECTRA

2.1. *ISO SWS*

The *ISO* Short Wavelength Spectrometer (SWS) is described by de Graauw et al. (1996), Vanetijn et al. (1996), and Schaeidt et al. (1996). The observations discussed here were made primarily in the SWS01 mode, where the entire wavelength range of the spectrometer (2.4–45 μm) is scanned during an observation, but where the spectrum is undersampled, producing a lower spectral resolution. There is also an SWS06 mode, in which a smaller wavelength range was observed at full resolution, and we will present four of these spectra, observed from 16.5 to 24 μm, for comparison. The spectrograph detected the flux in four different major wavelength bands, labeled bands 1–4, which each use different detectors. These were further subdivided into a total of 11 contiguous bands (1A, 1B, etc.), which involved different spectral orders and used different filters. The sizes of the *ISO* apertures, as projected on the sky, are 20″ × 14″ in bands 1 and 2, 27″ × 14″ in band 3 except for band 3E, 27″ × 20″ in band 3E, and 33″ × 27″ in band 4. The SWS01 observations discussed here were carried out with a variety of scan speeds, which vary the spectral resolution and sensitivity. Most of our SWS01 observations were carried out with the least wavelength sampling (speeds 1 and 2), with the resulting average effective resolution $R' = R/8 = \lambda/\Delta\lambda \sim 250$, where R is the maximum obtainable value. These observations were carried out as part of the Guest Observer program. In Table 2 we present a log of the observations.

2.2. *SWS01 Data Reduction*

The SWS01 data reduction presented here was carried out using version 7 of the standard pipeline processing. Once the autoanalysis results files had been obtained, they

TABLE 2

ISO OBSERVING LOG

IRAS ID	*ISO* Coordinates R.A. (2000.0)	decl. (2000.0)	Roll Angle[a] (deg)	Date of Observation (s)	Duration of Observation	Reset Time (s)	Resolution	*ISO* Program[b]
			SWS01					
01005+7910.....	01 04 45.69	+79 26 47.0	8.50	1997 Oct 1	2124	2	R/8	1
02229+6208.....	02 26 41.81	+62.21 22.2	250.60	1997 Feb 6	1352	1	R/8	1
02229off.....	02 26 59.01	+62.22 22.1	250.65	1997 Feb 6	1192	1	R/8	1
05341+0852.....	05 36 55.00	+08 54 09.0	94.44	1997 Oct 12	3666	2	R/4	2
07134+1005.....	07 16 10.17	+09 59 47.4	103.44	1997 Nov 7	3666	2	R/4	3
18576+0341.....	19 00 10.52	+03 45 49.2	264.94	1996 Oct 6	1352	1	R/8	4
19306+1407.....	19 32 55.00	+14 13 40.0	75.22	1997 Apr 24	2124	2	R/8	1
19477+2401.....	19 49 54.31	+24 08 47.1	60.91	1996 May 16	2046	2	R/8	4
20000+3239.....	20 01 59.45	+32 47 33.7	58.40	1996 May 20	1274	1	R/8	1
22574+6609.....	22 59 18.32	+66 25 48.6	251.29	1996 Dec 16	2124	2	R/8	4
			PHOT-S					
01005+7910.....	01 04 45.70	+79 26 47.0	8.48	1997 Oct 1	1344	...	...	2
02229+6208.....	02 26 41.80	+62.21 22.0	88.98	1997 Jul 16	576	...	...	2
19306+1407.....	19 32 55.00	+14 13 40.0	75.20	1997 Apr 24	1344	...	...	2
20000+3239.....	20 01 59.50	+32 47 33.0	81.80	1997 Apr 19	576	...	...	2

NOTE.—Units of right ascension are hours, minutes, and seconds, and units of declination are degrees, arcminutes, and arcseconds.

[a] *ISO* Roll angle is the orientation of the aperture from north through east, from what we have defined as the x-direction toward the y- direction.

[b] *ISO* Programs: (1) BHRIVNAK.SWSPPN01, (2) BHRIVNAK.SWSPPN03, (3) KVOLK.21MICPO, (4) BHRIVNAK.SWSPPN02.

were further analyzed using the *ISO* Spectral Analysis Package (ISAP). In this step, the obviously bad data points were removed and then the full set of data values was averaged to produce the final spectrum with a uniform wavelength spacing in bands 1–3D and in bands 3E and 4. For most of our sources the band 4 data values were severely affected by glitches, and it was not always possible to remove these in a satisfactory manner. This then led us in most cases to bin the data with a courser wavelength spacing in band 4 to improve the signal-to-noise ratio and to reduce the affect of residual "tails" of the glitches. The spectra presented have been binned at a constant wavelength interval of 0.05 μm for SWS bands 1, 2, and 3A–3D (2.4–27.5 μm). For $\lambda < 5$ μm, this treatment causes a loss of resolution even for SWS01 observations, but our sources have little signal at these wavelengths. For bands 3E and 4 (27.5–45.2 μm), the data for the brightest two sources were binned at a similar resolution of 0.05 μm, but for the others the data were binned at 0.20 μm. The data from 4 to 7 μm were usually noisy; this wavelength interval is near the flux minimum for most of the sources, and occasionally the resulting flux level came out negative in the reduction. This part of the processing was done on our local computers using a copy of ISAP 1.6 obtained from the Infrared Processing and Analysis Center (IPAC) in Pasadena.

In most cases our SWS01 data have problems in band 3E, 27.5–29.0 μm. This part of band 3 uses a larger aperture than the rest of the band 3 scans and seems to be subject to more noise. The response function is comparatively poor in this part of the band. Thus in most cases we do not trust the spectral data in band 3E.

2.3. *SWS Flux Calibration Issues*

In our initial reductions of the *ISO* SWS01 observations (prior to 1997 November), there was a drastic disagreement between the continuum levels from the *ISO* observations and those from previous *IRAS*, ground-based, or KAO observations. Most of these disagreements were removed when the *ISO* calibration files were updated in 1997 November. We will comment specifically on the agreement between the *ISO* SWS01 data and other mid-infrared data as we discuss the individual objects later. At present, we will discuss in detail the comparison of the *ISO* SWS01 spectra of two best-studied sources, IRAS 07134+1005 and 20000+3239, with other spectral data for these objects in the wavelength range 16–24 μm. For both of these objects, we have recently published spectra from 16.5 to 24 μm obtained with the *ISO* SWS in the SWS06 mode, which gives the full spectral resolution (Volk, Kwok, & Hrivnak 1999, hereafter VKH99). The *IRAS* LRS spectra are taken from the *IRAS* database at the University of Calgary.

Since the *IRAS* LRS spectra do not have an absolute flux calibration, the primary comparison of the *ISO* flux density is with the *IRAS* photometric data. Synthetic photometry was calculated from the *ISO* spectra using the ISAP reduction program. The *IRAS* Point Source Catalog (PSC) and the simulated *ISO* flux densities at 12 and 25 μm for each of our program objects are listed in Table 3. The agreement between the two data sets is good in general; specific comparisons will be made as we discuss the spectra of the individual objects. The *IRAS* LRS spectra are shown primarily to compare the spectral shapes.

IRAS 07134+1005 has a very strong 21 μm emission feature and can well be regarded as the prototype for this emission feature (VKH99). The synthetic photometry of the *ISO* SWS01 spectrum agrees well with the *IRAS* photometry at 25 μm but is 18% lower at 12 μm. The upper panel of Figure 1 shows our *ISO* SWS01 spectrum, together with the SWS06 spectrum (VKH99), the *IRAS* LRS spectrum (KVH89), the United Kingdom Infrared Telescope (UKIRT) CGS3 spectrum (Justtanont et al. 1996), and the KAO spectrum (O95). The various data sets have not been shifted in any way. There is excellent agreement between the SWS01 and *IRAS* LRS spectra for IRAS 07134+1005 from 7.6 to 19.5 μm, after which the LRS spectrum falls systematically below the SWS01 spectrum. The 21 μm feature is thus actually stronger in the SWS01 data than it appeared to be in the LRS data. The SWS06 spectrum shows the same shape as the SWS01 spectrum, except for a bump in the SWS01 spectrum at 17.8 μm that is much weaker in the SWS06 spectrum. There is also a bump at 18.9 μm in both the SWS01 and SWS06 spectra that has a different shape in the two data sets. Otherwise, the main difference between the two spectra is that the level is consistently $\sim$10% higher in the SWS01 spectrum than in the SWS06 spectrum. This is at the level of precision of the *ISO* SWS calibration (Schaeidt et al. 1996). The UKIRT CGS3 data are consistently below the SWS01 spectrum, by about 15% at 16–24 μm. This difference could in part be due to the smaller aperture (5".5) used with CGS3, since the source is known to be extended in the mid-infrared, with a full-width at half-maximum (FWHM) of $\sim$3".3 and a full-width at zero-

TABLE 3

COMPARISON OF *IRAS* AND SIMULATED *ISO* PHOTOMETRY

	OBSERVED *IRAS* PSC FLUX DENSITIES[a]		SIMULATED FLUX DENSITIES FROM *ISO* DATA	
OBJECT	F_{12} (Jy)	F_{25} (Jy)	F_{12} (Jy)	F_{25} (Jy)
01005+7910.....	3.9 ± 3%	24.2 ± 5%	2.7	15.9
02229+6208.....	66.7[b]	203.7[b]	64.3	241.8
05341+0852.....	4.5 ± 4%	9.9 ± 7%	2.9	8.0
07134+1005.....	24.5 ± 5%	116.7 ± 4%	20.2	118.5
18576+0341.....	58.5 ± 6%	425.0 ± 5%	16.9	200.4
19306+1407.....	3.6 ± 6%	58.6 ± 4%	3.2	61.0
19477+2401.....	11.2 ± 5%	54.9 ± 4%	1.5	18.8
20000+3239.....	15.0 ± 6%	70.8 ± 4%	13.8	66.1
22574+6609.....	9.0 ± 3%	29.5 ± 4%	7.2	26.1

[a] Errors shown are percentages.

[b] IRAS Z02229+6208 is not included in the *IRAS* PSC; values are from Hrivnak & Kwok 1999.

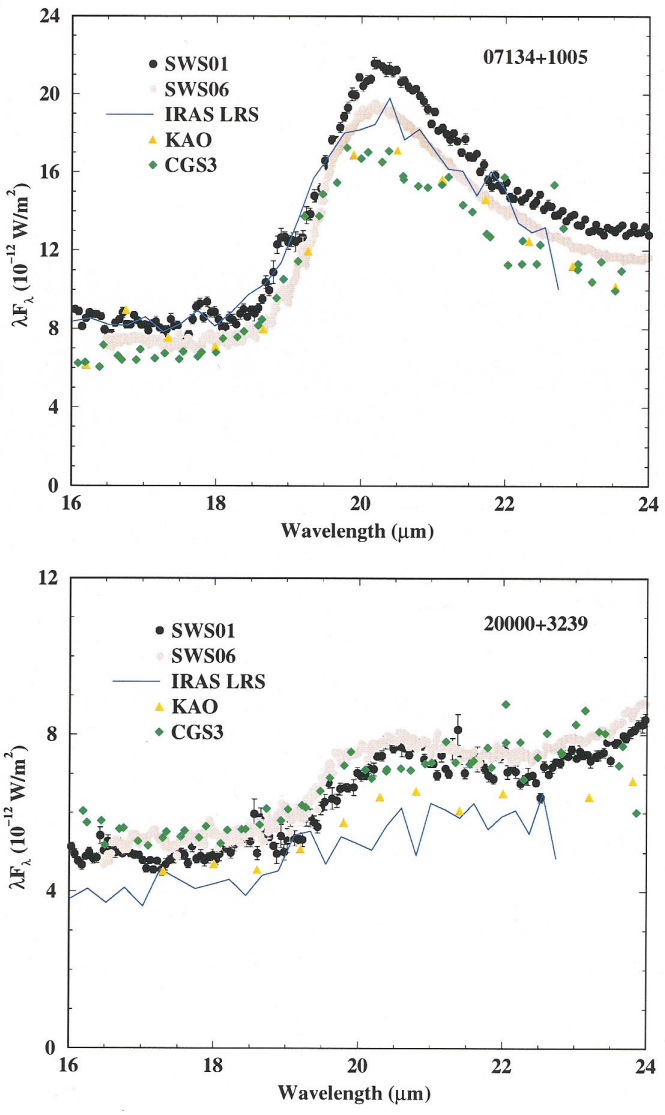

FIG. 1.—Comparison of the *ISO* SWS01 spectra of (*upper panel*) IRAS 07134+1005 and (*lower panel*) IRAS 20000+3239 with other measurements in the 16–24 μm region.

intensity of ~7″ (Meixner et al. 1997; Dayal et al. 1998). The data from the KAO (30″ aperture) fall about 10% below the SWS01 data at shorter wavelengths (16–19 μm), thus agreeing well with the SWSO6 data. However, at wavelengths greater than 19.5μm the KAO spectrum drops relatively lower, matching the CGS3 data. Since the position of this object is well established, pointing should not be a problem. We think that the differences in flux levels, as shown in the upper panel of Figure 1, basically reflect the levels of the precision in the calibrations of the various instruments.

IRAS 20000+3239 is also a source that has been observed with the *ISO* SWS06 (VKH99), KAO (O95), and UKIRT CGS3 in addition to the *IRAS* LRS (Kwok, Hrivnak, & Geballe 1995, hereafter KHG95). While the values from the *IRAS* photometry and the *ISO* synthetic photometry are similar, the *IRAS* LRS spectrum of IRAS 20000+3239 is consistently below the SWS01 flux level, by about 20% at 16 μm. The agreement is very good between the *ISO* SWS01 and SWS06 spectra. These are shown in the lower panel of Figure 1. The UKIRT CGS3 spectrum (KHG95) agrees well with the SWS01 spectrum over the entire range in common. The KAO spectrum is slightly below (~15%) the SWS01 from 16 to 28 μm. IRAS 20000+3239 is smaller in size, FWHM ~ 1.″2 (Meixner et al. 1999), and thus its flux levels would be less affected by the differences in aperture size.

Based upon these detailed comparisons, there appear to be no obvious problems with the *ISO* SWS01 flux calibration.

2.4. *Possible Centering Errors and Aperture Effects*

The SWS01 data for two sources, IRAS 18576+0341 and 19477+2401, show a strange discontinuity at the end of band 3D (27.5 μm), with the flux density in bands 3E and 4 much higher. To provide continuity in the spectrum of IRAS 19477+2401, the flux density values in bands 1, 2, and 3A through 3D have been scaled by a factor of 2.92 for this object; this scale factor was determined from the ratio of the *IRAS* 25 μm flux density and that deduced from the SWS01 spectrum in ISAP. For IRAS 18576+0341, the data were scaled by a factor of 1.82; this scaling factor was chosen to produce a smooth continuum shape. This also produces agreement between the *ISO* SWS01 spectrum and the broadband photometry at *L* and *M* for IRAS 18576+0341.

In both cases we believe that the cause of the discontinuity in the spectrum is that the objects were not properly centered in the *ISO* aperture. This is a distinct possibility for both of these sources, since they have faint (IRAS 19477+2401, $V = 22.2$) or no (IRAS 18576+0341, $V > 23.2$) observed visible counterparts. Their positions were determined from our ground-based mid-infrared photometry, which we had assumed to be accurate to 1″–2″. In Table 2 are listed the *ISO* positions used in the observations. The scaling factors of 2–3 suggest that the two sources were actually partially beyond the edge of the *ISO* apertures for bands 1, 2, and 3A to 3D. When the larger apertures for bands 3E and band 4 were used, the observed flux density levels were higher.

If one treats the *ISO* aperture sizes (listed in § 2.1) as if they were the dimensions in the *x*- and *y*-directions, respectively, then in order that there be an aperture effect between band 3 and band 4 but not between band 2 and band 3, the object must have been near the edge of the aperture in the *y*-direction but near the middle of the aperture for bands 1 and 2 in the *x*-direction. If this were the case, then when the aperture *x*-dimension increases between band 2 and band 3 there would be no significant change in the continuum because the "missing" flux density comes from the inner regions of the dust shell at short wavelengths and this part of the object is still partially cut off by the edge of the aperture. Then, when observing in bands 3E and 4, all the inner regions of the dust shell are visible because of the enlarged aperture in the *y*-direction.

To examine this idea quantitatively, we carried out source brightness calculations at the wavelengths at which the radiative transfer model is calculated, assuming a spherical dust shell (see § 4). From these source brightness curves we then simulated the aperture blockage for a given offset in *y* from the center of the apertures, and sought to match the observed ratios between the various bands. For IRAS 18576+0341 a good match was obtained for a *y* offset of 6.″8. This value is uncertain by ≈0.″1 because of uncertainties in the model. The models indicate that the

circumstellar shell of this object is relatively large in sky area, with a best-fit inner angular radius of 2.″85. The geometry we have in mind for IRAS 18576+0341 is shown in Figure 2, using the source brightness at 22.3 μm from the best-fit model as an example. The source brightness peaks at the inner edge of the dust shell.

For IRAS 19477+2401, the scaling factor is 2.92. Carrying out the same type of modeling as for IRAS 18576+0341 gives a best fit offset in the *y*-direction of 7.″1. This object appears to be much farther away than is IRAS 18576+0341, and the model fitting is better. Therefore this offset value appears to be quite accurately determined. In fact, IRAS 19477+2401 has recently been observed with the *Hubble Space Telescope* (*HST*), and its *HST* position (R.A. = $19^h49^m54^s.9$, decl. = +24°08′ 53.″1, 2000.0) differs from the observed *ISO* position by +8″ in right ascension and +6″ in declination. This is consistent with the offset determined above.

2.5. *ISO PHT-S Spectra*

The *ISO* imaging photopolarimeter and spectrophotometer ISOPHOT is described by Lemke et al. (1996). Observations were made of four of these sources in the spectrophotometer (PHT-S) mode, and these are also listed in Table 2. The spectra are in two wavelength ranges, 2.5–4.9 μm and 5.9–11.6 μm, with resolutions of 0.045 and 0.095 μm, respectively. The observations were carried out in staring mode for the two brighter sources, IRAS Z02229+6208 and 20000+3239, and in chopped mode for the two fainter sources, IRAS 01005+7910 and 19306+1409.

The data were reduced using the PHOT Interactive Analysis (PIA) program version 7.3.2 at IPAC. Photometric calibration techniques are discussed by Schultz et al. (1999) and by U. Klaas et al. (2000, in preparation). The standard processing procedure was used except for the photometric calibrations; the absolute calibration was carried out using dynamical calibration for the staring observations and using the special chopped mode calibration for the chopped observations. The default calibration, using an averaged staring mode calibration file, produces bad results for chopped mode observations in particular. Comparison was then made with the SWS01 data from bands 1 and 3 for all four sources. In all cases the PHT-S and SWS01 spectra agree well in shape where the source is bright enough that the SWS01 data are trustworthy. The PHT-S data are particularly valuable as a supplement to the SWS01 band 2 data, which are usually of poor quality for these sources, and for detection of features at the shortest wavelengths, such as the 3.3 μm UIR feature. The agreement in flux density level is good for all the sources except for IRAS 20000+3239, for which the PHT-S spectrum is 30% higher than the SWS01 spectrum. Comparison with broadband photometry showed that the PHT-S observations for IRAS 20000+3239 were too high in flux density while the SWS01 observations agreed with the photometry. Therefore, a scale factor of 0.76 was applied to the PHT-S data for this object and produced good agreement with the SWS01 data.

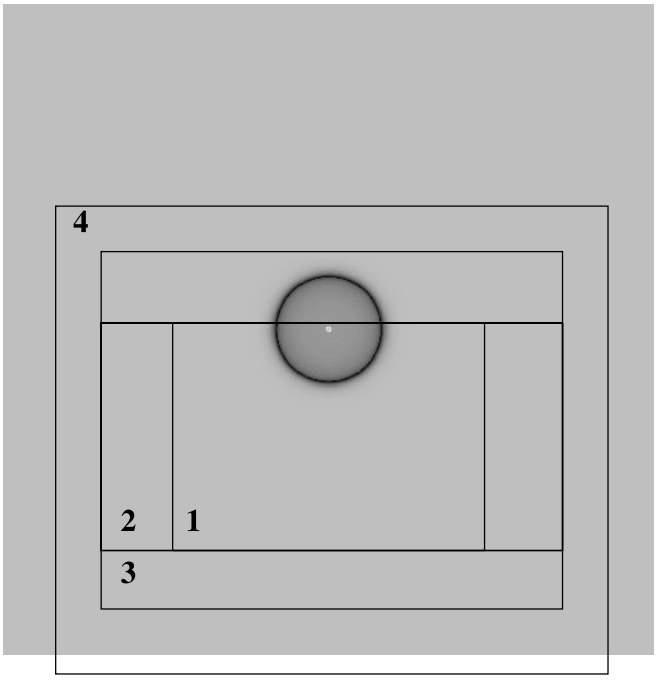

FIG. 2.—Aperture effects in the observation of IRAS 18576+0341. The gray-scale image is a model presentation of the dust shell brightness. Superimposed are the sizes of the *ISO* apertures to the same scale, with the correct offset to reproduce the aperture effects seen in the SWS01 spectrum. Aperture 1 (20″ × 14″) is for bands 1 and 2, aperture 2 (27″ × 14″) for band 3A to 3D, aperture 3 (27″ × 20″) is for band 3E, and aperture 4 (33″ × 27″) is for band 4.

2.6. *Spectra of Individual Objects*

The complete *ISO* SWS01 spectra of all nine objects are displayed in Figure 3. The spectral region from 2 to 15 μm is shown in more detail in Figure 4, including the PHT-S spectra of the four sources observed.

07134+1005 (*HD 56126*).—The *ISO* spectrum for this source was obtained at a scan speed of 3. It is of very good quality from 8 to 27.5 μm, but of poorer quality at the longer wavelengths (bands 3E and 4). The 21 μm feature is very strong, as has been discussed above. Also seen is a plateau from 11 to 18 μm and probably a broad 30 μm feature, although it appears less prominent than in some of our other sources.

Narrow emission features are seen at 7.5 μm (weak), 11.3 μm, 12.1 μm (weak), and perhaps 12.4 and 13.3 μm (both weak). The 7.5 μm feature is on a broad emission region that extends from 6.7 to 9.5 μm. There appears to exist a weak emission feature at 7.0 μm. Most of these same features have previously been seen in this source in UKIRT CGS3 spectra (8, 11.3, 12.2, 21 μm: Justtanont et al. 1996) and KAO spectra (6.9, 7.7 μm: Buss et al. 1990; 21, 30 μm: O95). There also appear to be new emission features at 18.9 and 26.4 μm and possibly at 17.8 μm. The feature at 18.9 μm can be seen in more detail in the upper panel of Figure 1 and is also evident in the SWS06 spectrum shown for comparison; however, it does not appear in the UKIRT CGS3 spectrum of Justtanont et al. (1996). The reality of the feature at 26.4 μm is supported by the presence of a weak emission feature at this wavelength in the KAO spectrum (O95), and, as we discuss below, the presence of this feature in most of our other sources. An examination of the short wavelength end of the spectrum shows an increase in the flux density from 4 through 2.4 μm, as the contribution of the reddened stellar photosphere becomes significant. A discussion of the agreement of the *ISO* SWS01 spectrum with previous data is given in § 2.3 above. We note that the KAO data appear to have a calibration problem at wavelengths greater than 19 μm, appearing basically to be too flat.

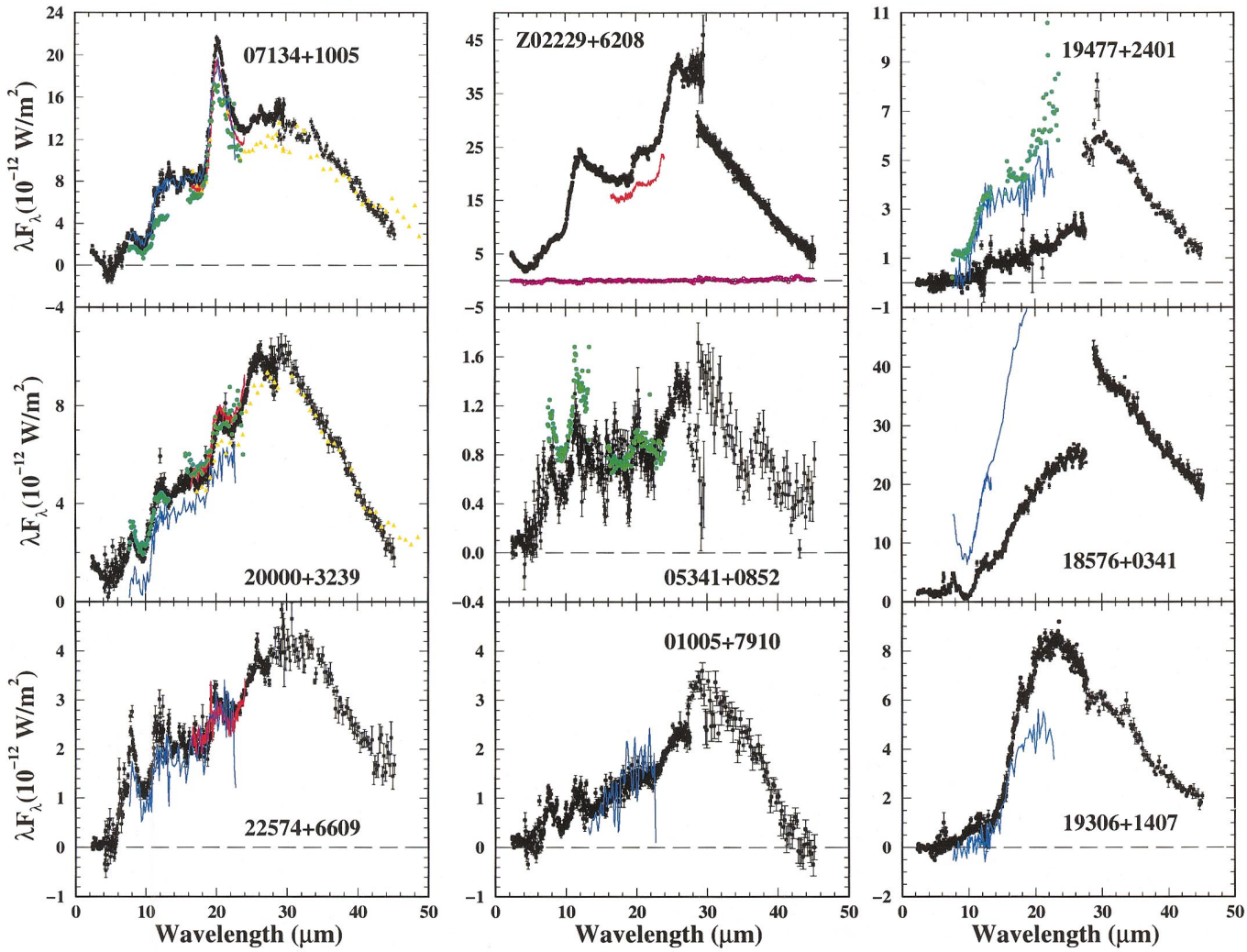

FIG. 3.—*ISO* SWS01 spectra (*black squares*), plotted with error bars. Plotted for comparison are *IRAS* LRS (*blue lines*), UKIRT CGS3 (*green circles*), KAO (*orange triangles*) and *ISO* SWS06 (*red lines*) spectra. Also plotted for Z02229+6208 is the offset spectrum (*purple*; see text for details). No scaling factors have been applied to the *ISO* data.

20000+3239.—The *ISO* spectrum is of good quality from 2.4 to 4 μm and longward of 6 μm. Several emission features can be seen: features at 3.3, 6.3, 6.9, 11.5, and 12.1 μm, a relatively broad 8 μm feature, the 21 μm feature, and the broad 30 μm feature. The longer wavelength features have been seen previously in UKIRT CGS3 (KHG95) and KAO (O95) spectra of the source, but the three shortest ones are new detections. There also appears to be a weak emission feature at 23 μm, seen in both the SWS01 and SWS06 spectra, and an emission feature at 26.3 μm. A comparison of the previous mid-infrared spectra with the *ISO* SWS01 spectrum has been discussed above. The KAO spectrum agrees well with the SWS01 from 30 to 43 μm and then is somewhat higher beyond 43 μm. From 5 to 2 μm, one can see the increasing flux of the stellar photosphere. The decrease in flux shortward of 2.5 μm may be due to the CO absorption band, which is known to be strong in this source (Hrivnak, Kwok, & Geballe 1994).

22574+6609.—This source is not as bright as the previous two, and the quality of the *ISO* spectrum is not as good. Nevertheless, a number of emission features are seen: at 6.2 μm, 6.9 μm, 7.8 μm (very strong) on a broad emission region at 8 μm, 11.3 μm, 12.0 μm, and perhaps 12.4 μm. There are also emission features at 13.3, 19.3, and 25.8 μm. (Note that the 19.3 μm feature is also found in the SWS06 spectrum but was initially thought to be a glitch in the data; VKH99.) Also present are the 21 μm feature and the broad 30 μm feature. The 21 μm feature had been tentatively identified in the noisy *IRAS* spectra, along with the 8 μm feature and the plateau from 11 to 19 μm (Hrivnak & Kwok 1991). The new *ISO* spectra confirm the presence of the 21 μm feature in this object, and agree well with each other (VKH99). The normalized 21 μm profile also agrees well with the others shown in VKH99. The LRS spectrum (Hrivnak & Kwok 1991) agrees very well with the *ISO* SWS01 spectrum, although it does not have the sensitivity or spectral resolution to show the weaker features seen here. The SWS01 spectrum is very weak from 2.4 to 4 μm, and from 4 to 6 μm it is very noisy. The *ISO* synthetic photometry values are 20% and 10% below the *IRAS* values at 12 and 25 μm, respectively (see Table 3).

Z02229+6208.[2]—The *ISO* spectrum is of good quality and has been binned throughout at 0.05 μm. A very strong

[2] The "Z" added before the *IRAS* ID designates that the object is not found in the *IRAS* Point Source Catalog but is rather found in the *IRAS* Faint Source Reject File. For more details about this object and its discovery, see Hrivnak & Kwok (1999).

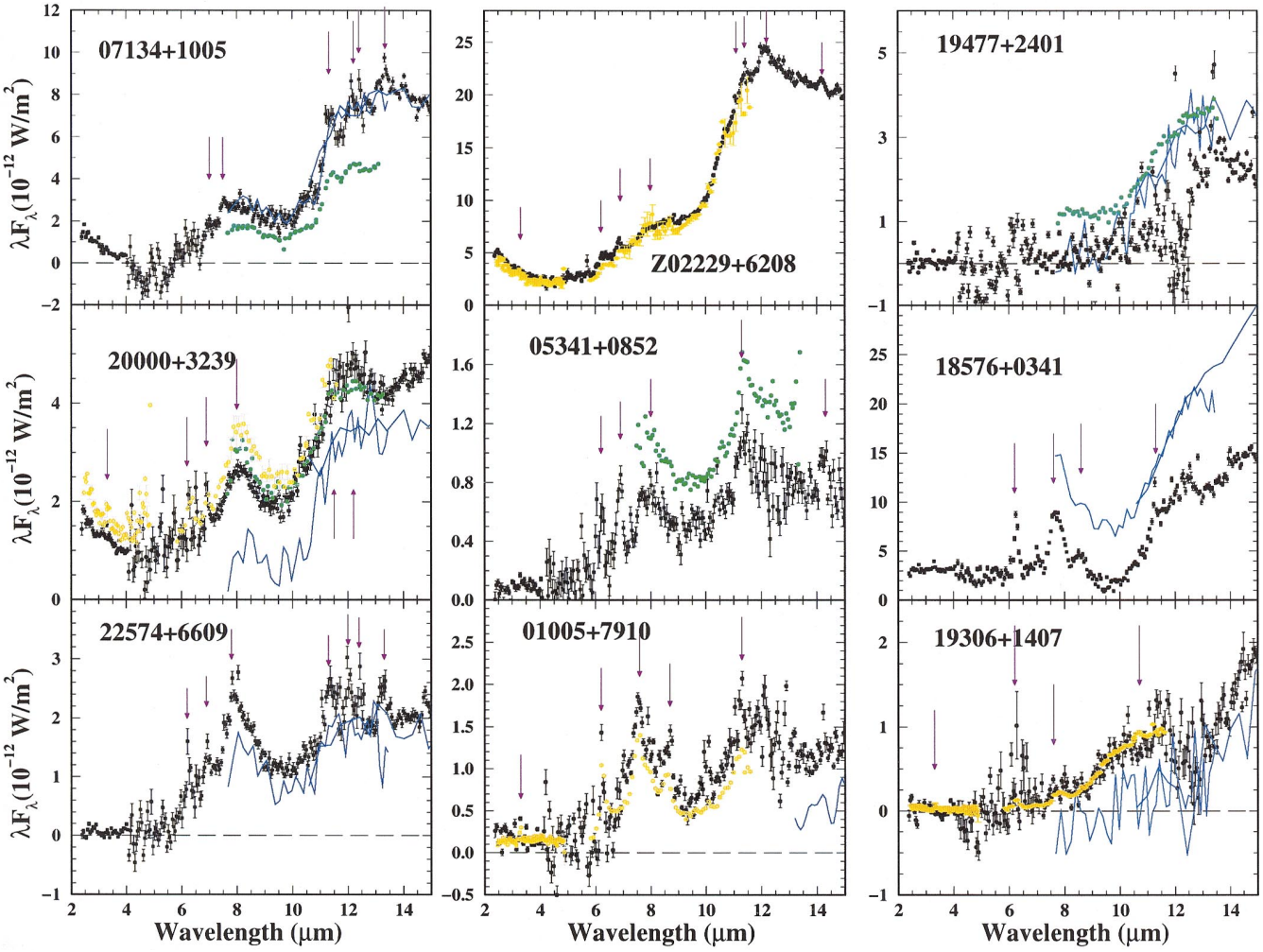

FIG. 4.—Expanded plot of the *ISO* SWS01 spectra in the 2–15 μm region, with *ISO* PHT-S (*orange circles*) spectra included, and spectral features marked by arrows. Other symbols are the same as in Fig. 3. The *ISO* flux densities for IRAS 01005+7910, 19477+2401, and 18576+0341 have been scaled by factors of 1.50, 2.92, and 1.82, respectively, as discussed in the text.

emission plateau is seen from 10.2 to 19 μm, followed by a weak 21 μm feature on a steeply rising continuum up to very strong peak at 26 μm. The noisy region at 28 μm lies entirely within band 3E, which is known to have problems, and thus we do not trust the reality of the apparent feature. However, the strong feature at 26.1 μm does appear to be real and is seen, albeit more weakly, in most of our other sources. An examination of a sample of oxygen-rich PPNs does not show a feature at this wavelength, so we think that it is a real feature peculiar to carbon-rich sources. There may also be a 30 μm feature, which our modeling confirms. A discontinuity of $\sim$10% is seen in the spectrum at 19.5 μm, which is an edge between bands 3C and 3D and is presumably due to some slight calibration problem. The SWS06 spectrum (VKH99) shows a 21 μm feature with a similar shape and strength, if a correction is made to join the sections of the SWS01 spectrum at 19.5 μm. However, the SWS06 spectrum is 25% weaker than the SWS01 spectrum. This difference is larger than the expected calibration uncertainty. These two *ISO* spectra were obtained 4 days apart, and we do not expect source variability on this timescale. To seek to understand this difference in flux density, we compared the *ISO* synthetic photometry with the *IRAS* photometric values. The *ISO* SWS01 flux density level agrees well with the *IRAS* 12 μm flux density level but is 20% too high at 25 μm, while the SWS06 spectrum is in good agreement with the *IRAS* 25 μm flux density. Thus there are inconsistencies between the *ISO* SWS01 and SWS06 spectra and between the *ISO* and the *IRAS* flux densities for this object.

Narrow emission features are seen at 6.9 μm and possibly at 3.3 and 6.3 μm, followed by a broad emission region from 7.3 to 9.5 μm. Weak emission features are seen at 11.1, 11.4, and 12.2 μm, superimposed on the strong emission plateau. There also appear to be emission features at 14.2 and 24.2 μm. At the shortest wavelengths, one sees an increase in the flux density from 4 to 2.5 μm, which is attributed to the photosphere of the star. The decrease in flux density from 2.5 to 2.4 μm may be real and due to the 2.3 μm CO bandhead. These *ISO* spectra are the first mid-infrared spectra obtained for this object, so there are no other previous spectra with which to compare it.

Because the source is in the direction of a cool H II region (W3N) that was known to affect the longer *IRAS* flux measurements (Hrivnak & Kwok 1999), we also obtained an *ISO* spectrum offset 2′ NE of the source to measure the background. This offset spectrum is quite weak; it shows essentially no flux at wavelengths less than 24 μm and rises

to a maximum of ~10% of the source spectrum at the longest wavelengths. The only structure is possibly a weak feature at 30 μm. We decided not to subtract this weak background spectrum from that of the IRAS Z02229+6208 spectrum presented here. This offset spectrum is shown in Figure 3.

05341+0852.—The *ISO* spectrum was obtained at a scan speed of 3. IRAS 05341+0852 is much fainter than the other objects in this study and the spectrum is rather noisy. Nevertheless, emission features can be seen at 6.2 (weak) and 6.9 μm and strong emission features at 8 and 11.3 μm. These strong features are also seen in the UKIRT CGS3 spectra (KHG95; Justtanont et al. 1996). There also appear to be features at 14.3 μm and 26 μm, and perhaps there is evidence for the broad 30 μm feature. The 21 μm feature may be present in the *ISO* spectrum, although it appears less convincing than in the UKIRT CGS3 spectrum (KHG95). The *ISO* spectrum rises smoothly from 22 to 27.5 μm, then the region of band 3E, from 27.5 to 29 μm is quite noisy and unreliable, and then beyond 30 μm the spectrum is again noisy but appears generally to trace the continuum. The flux density levels of the *ISO* and CGS3 spectra agree well in the 16–24 μm region, but the CGS3 spectrum is 60% brighter in the shorter wavelength region (7–13 μm). Comparison with the *IRAS* 12 μm flux density indicates that it is the *ISO* spectrum that is too low at 12 μm. On the other hand, in the shorter wavelength region the shapes are similar between the *ISO* and the CGS spectra, but less so in the longer wavelength region.

01005+7910.—The *ISO* spectrum of IRAS 01005+7910 is faint and rather noisy. This is especially true of the longer wavelength region and the SWS01 spectrum below 7 μm. However, the PHT-S data have a much higher signal-to-noise ratio, and this allows us to detect an emission feature at 3.3 μm, in addition to the strong feature at 7.7 μm and additional features a 6.2, 8.6, and 11.3 μm. There also appears to be a feature at 26 μm, which appears somewhat broader than that seen at 26 μm in the other sources. The spectrum is of very poor quality in band 3E, with large error bars. The flux density level in the *ISO* spectrum is ~30% below the *IRAS* photometric values, and there also appears to be a discontinuity in the *ISO* spectrum at 27.5 μm. This suggests that a scaling factor of 1.5 be applied to the *ISO* shorter wavelength (2.4–27.5 μm) spectrum to make it agree with the *IRAS* photometry and also produce a smooth *ISO* spectrum. The *IRAS* LRS spectrum has been extracted and examined; it is very noisy at the short wavelengths (and thus we have not plotted this region) but appears approximately similar to the *ISO* spectrum from 13 to 23 μm.

19477+2401.—This is a weak source that has been observed previously with the *IRAS* LRS and with the UKIRT CGS3. As discussed earlier in § 2.4, a sharp discontinuity in the spectrum occurs at 27.5 μm, which we attribute to aperture effects caused by the source being offset from the observation position. In Figure 3 the observed spectrum is displayed, showing this discontinuity; the scaled spectrum is shown in Figure 4. Comparisons can be made with *IRAS* LRS (extracted) and CGS3 (KHG95) data. The shapes of the spectra appear similar. The scaled *ISO* spectrum is still fainter than the *IRAS* and CGS3 spectra by ~50% at 13 μm. Below 13 μm, the *ISO* spectrum is quite faint and is very noisy from 11.5 to 12.7 μm. This severely hinders one from determining whether emission features are present at short wavelengths. An emission feature is seen at 26 μm, and there may be a weak emission feature at 20 μm, possibly the 21 μm feature. The 30 μm feature also appears to be present.

18576+0341.—This is a very strong source, and the spectrum has been binned throughout at 0.05 μm. It shows a number of emission features. The sharp discontinuity in the spectrum at 27.5 μm, attributed to an aperture effect, can be clearly seen. This is corrected by applying the calculated scaling factor of 1.82 to the flux density at wavelengths less than 27.5 μm (bands 1 to 3D) to produce a smooth spectrum. This scaled spectrum is shown in Figure 4, where it is compared with the *IRAS* LRS spectrum. The two spectra have the same general shape. Although the *ISO* spectrum is noisy from 4 to 7 μm, nevertheless a strong emission feature is seen at 6.2 μm. There is a strong emission feature at 7.6 μm, features at 8.6 and 11.3 μm, and an emission plateau from 11 to 13.3 or to perhaps 14 or 15 μm, depending on where the continuum level is assumed to be. The 11.3 μm feature is narrower than in the other sources, but we judge it to be real. Weak emission features appear to be present at 16 and 17 μm on a steeply rising continuum. It is unclear if the series of peaks and troughs seen in the spectrum from 20 to 27 μm are real or due to inadequate removal of fringing in the spectrum. The scaled spectrum peaks at ~27 μm. There does not appear to be a broad 21 or 30 μm emission feature in the spectrum. Even with this scaling up of the spectrum below 27.5 μm, it still falls below the *IRAS* 12 and 25 μm flux density. It may be that object is relatively large in angular size and that some of the flux observed with *IRAS* is still outside of the largest *ISO* SWS aperture. The *IRAS* LRS spectrum has been published by Volk & Cohen (1989), who placed it in their class H, red continuum sources that are mostly H II regions, and note that it is a possible PN based on its *IRAS* color.

19306+1407.—The spectrum of this object shows an emission plateau from 9 to 12 μm, a steep rise from 13 to 20 μm, and peaks at ~23 μm. The PHT-S spectrum of this source has a much higher signal-to-noise ratio than does the SWS01 spectrum in this wavelength region. Emission features are seen at 6.3, 7.8, and 10.7 μm, with a probable feature at 3.3 μm also. There is also a possible emission feature at 17.8 μm, although it is hard to be certain since there is evidence of several similar "emission peaks" in the 20–24 μm region that we judge to simply be noise. The apparent emission feature at 34 μm we do not believe to be real; the spectrum is noisy in this region and many data points were removed in the processing. The *IRAS* LRS spectrum has been classified by Kwok, Volk, & Bidelman (1997) as class H. The LRS spectrum has a similar shape to the *ISO* SWS01 spectrum but is fainter, by 40% at 20 μm, although the *IRAS* photometry and *ISO* synthetic photometry values agree well.

2.7. *Summary of ISO Spectral Features*

In Table 4 we list the emission features identified in the *ISO* spectra of the individual objects. There are several features common to most of the objects. These include the UIR features at 6.2, 6.9, 7.7, and 11.3 μm, commonly attributed to PAHs. In some of the objects, rather than a 7.7 μm feature there appears to be a broad 8 μm (8br) feature instead. The four sources with PHT-S observations all show some evidence of the 3.3 μm emission feature, which had been seen previously in two others of these sources, IRAS 07134+1005 (Kwok, Hrivnak, & Geballe 1990) and IRAS

TABLE 4

LIST OF EMISSION FEATURES SEEN IN *ISO* SPECTRA

Object	3.3	6.2	6.9	7.7	8br	8.6	11.3	12.1	Other	"21"	"26"	"30"
01005+7910.....	Y	Y	N	Y	N	Y	Y	N	...	N	Y	Y
02229+6208.....	Y:	Y:	Y	N	Y	N	Y	Y	11.1, 14.2, 24.2	Y	Y	Y
05341+0852.....	(Y)[a]	Y	Y	N	Y	N	Y	N	14.3	Y:	Y	Y:
07134+1005.....	(Y)[b]	...	Y	Y	Y	N	Y	Y	12.4:, 13.3:, 17.8:, 18.9	Y	Y	Y
18576+0341.....	...	Y	N	Y	N	Y	Y	N	16:, 17:	N	N	N
19306+1407.....	Y:	Y	N	Y	N	N	N	N	10.7, 17.8	N	N	N
19477+2401.....	...	...	...	...	...	...	N	...	...	Y:	Y	Y
20000+3239.....	Y	Y	Y	N	Y	N	Y	Y	23	Y	Y	Y
22574+6609.....	...	Y	Y	Y	Y	N	Y	Y	12.4:, 13.3, 19.3	Y	Y	Y

[a] Detected in ground-based spectrum by Geballe & van der Veen 1990.
[b] Detected in ground-based spectrum by Kwok et al. 1990.

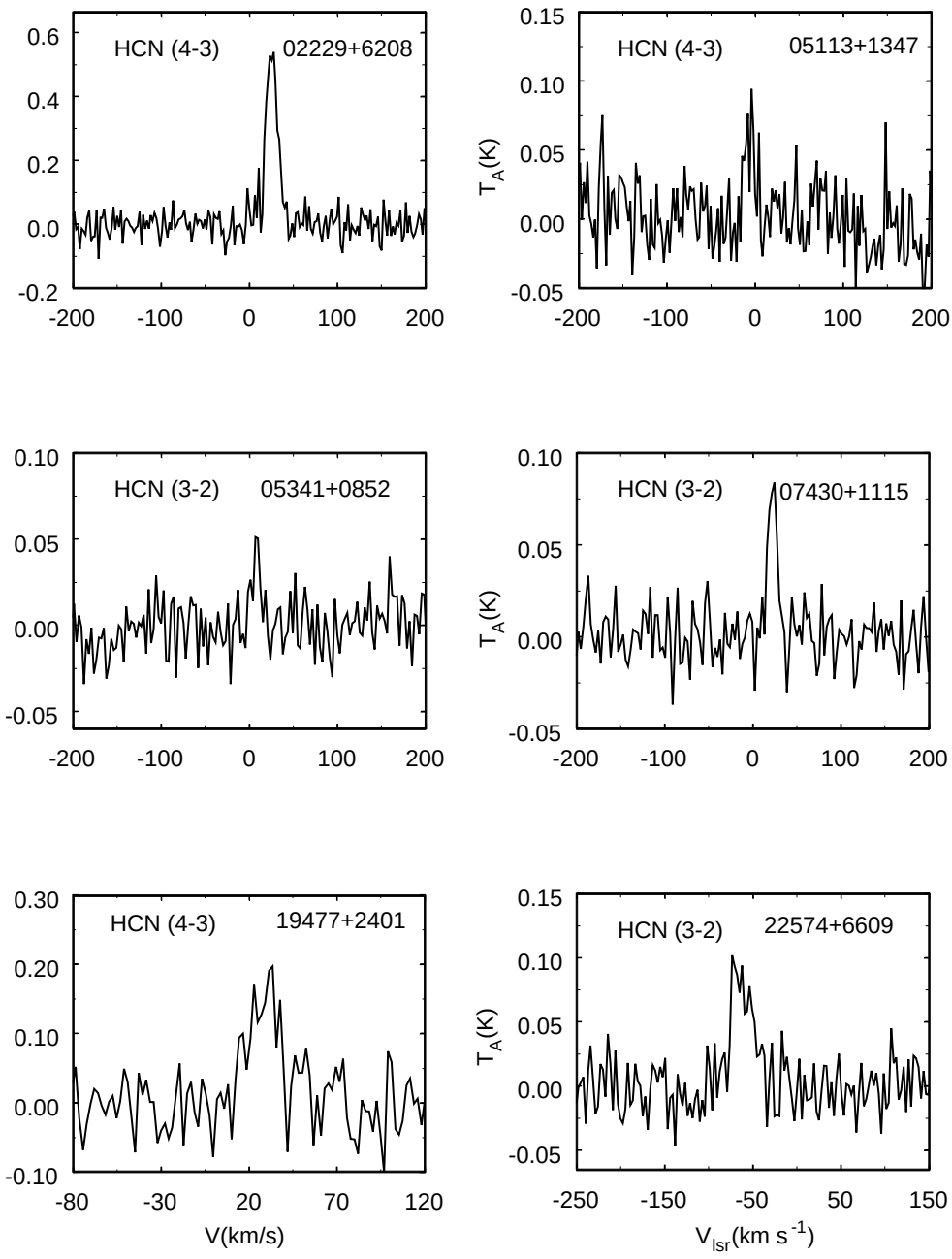

FIG. 5.—JCMT HCN spectra of six carbon-rich PPNs

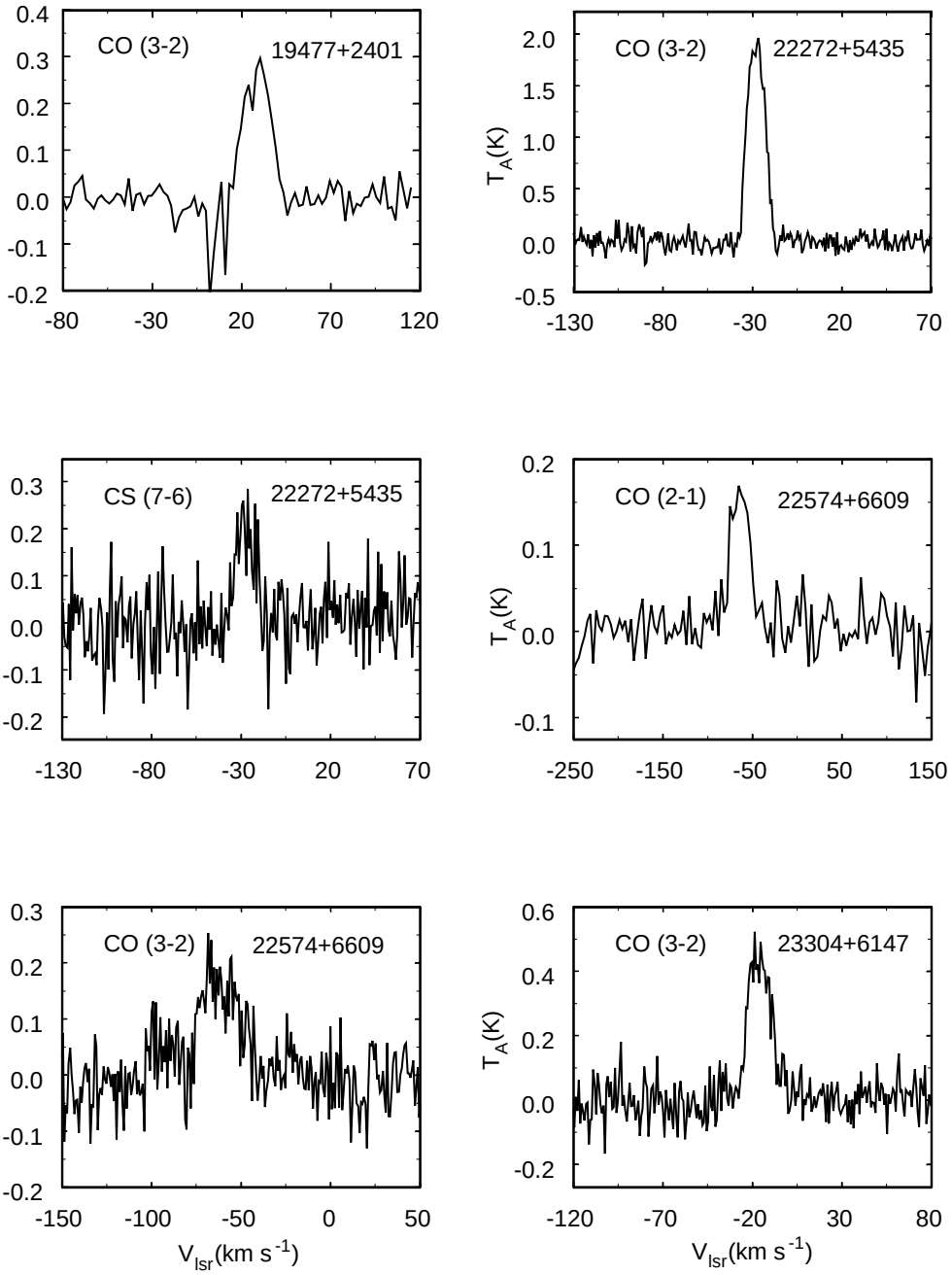

FIG. 6.—The JCMT CO and CS spectra of four carbon-rich PPNs

05341+0852 (Geballe & van der Veen 1990). A narrow feature at 12.1 μm is seen in four of the sources. Also present are the 21 and 30 μm features previously seen in evolved carbon-rich objects. *In almost all of the objects, a new emission feature at 26 μm is clearly present*, and in IRAS Z02229+6208, this feature is very strong. A discussion of the strengths of these features is given in § 5. In addition, there are other emission features that are seen in one or two objects but that are not in common to many of the objects. With this in mind, we would classify them as tentative identifications of emission features.

3. MILLIMETER MOLECULAR EMISSIONS

Studies of molecular-line emissions from PPNs provide very useful sources of information about the chemistry and kinematics of their circumstellar envelopes. Observations of several carbon-rich PPNs were carried out for this purpose at the James Clerk Maxwell Telescope in Hawaii on several dates from 1994 to the present. The lines observed were CO (2–1), CO (3–2), HCN (3–2), HCN (4–3), and CS (7–6).

The HCN observations were made primarily in 1998 and were taken using a beam switch of 180″ and 120″ in azimuth at 1 Hz for 265 and 354 GHz, respectively. The dual-channel SiS receiver B3 (in 1998 September) and A2 (in 1998 December) were used, together with an autocorrelation spectrometer. Typical integration times were 10 to 20 minutes. The spectrometer bandwidth was 250 MHz, resulting in a channel spacing of 313 kHz, and an effective resolution of 378 kHz, which corresponds to velocity resolutions of 0.32 and 0.43 km s^{-1} at 354.5 and 265.9 GHz,

TABLE 5

DERIVED MOLECULAR-LINE PARAMETERS

Object	Line	T_A(peak) (K)	V_{exp} (km s^{-1})	V_{lsr} (km s^{-1})	$\int T_A\, dV$ (K km s^{-1})	Date
02229+6208	HCN(4–3)	0.54 ± 0.04	14.8	+27.6	9.26	1998 Sep 23
05113+1347	HCN(3–2)	0.05 ± 0.02	16.9	−6.2	0.70	1998 Dec 26
05113+1347	HCN(4–3)	0.09 ± 0.02	17.0	−4.1	0.82	1998 Sep 23
05341+0852	HCN(3–2)	0.05 ± 0.01	11.3	+7.0	0.40	1998 Dec 26
07430+1115	HCN(3–2)	0.08 ± 0.01	14.1	+24.7	1.10	1998 Dec 26
19477+2401[a]	CO(3–2)	0.30 ± 0.03	17	+30.5	4.9	1999 Jul 27
19477+2401[a]	HCN(4–3)	0.20 ± 0.04	15	+33.5	3.2	1999 Jul 27
22272+5435	CO(3–2)	2.04 ± 0.04	9.8	−27.9	22.78	1994 Jun 24
22272+5435	CS(7–6)	0.22 ± 0.05	10.6	−27.3	3.61	1994 Jun 24
22574+6609	CO(2–1)	0.17 ± 0.03	26.0	−65.3	4.81	1998 Dec 26
22574+6609	CO(3–2)	0.18 ± 0.04	20.0	−62.3	20.05	1994 Jun 24
22574+6609	HCN(3–2)	0.10 ± 0.02	28.2	−73.4	2.54	1998 Dec 26
23304+6147	CO(3–2)	0.46 ± 0.04	17.4	−12.7	17.4	1994 Jun 24

[a] These measurements have a large uncertainty because of possible emission in the off-source position and poor weather conditions.

respectively. For receiver B3, which has dual polarizations, signals from both polarization channels were averaged together. All the spectra were binned over eight channels, with a resulting frequency resolution of 2.5 MHz. HCN was detected in six sources, all for the first time, including four of the program objects for which we present *ISO* spectra. The detection of HCN is consistent with their carbon-rich nature.

Observations of CO were made using a similar setup, and four objects were detected, including two with *ISO* spectra. For all four objects, this was the first detection in CO (3–2). In addition, CS (7–6) was detected for the first time in the carbon-rich PPN IRAS 22272+5435; CS (2–1) had previously been detected (Lindqvist et al. 1988). The spectra are plotted in Figures 5 and 6. The line shapes were fitted with Gaussians, and the derived line parameters are summarized in Table 5. The expansion velocities measured for most of the sources are in the range of 10–20 km s^{-1}, typical of AGB stars and PPNs. However, the value for IRAS 22574+6609 (26 km s^{-1}) is unusually high.

4. RADIATIVE-TRANSFER MODELS

In order to derive the properties of the "21 μm" and "30 μm" features, and also the distinct, new "26 μm" feature seen in several of the spectra, the *ISO* SWS01 spectra have been fitted with radiative-transfer models. These are based upon the DUSTCD code of Leung (1976), with some modifications specific to modeling circumstellar dust shells. We did not attempt to fit the narrower features nor the plateau features because of the uncertainty of whether the effects of quantum heating are important in the excitation of these features. The continuum and the broad features are probably due to solid-state materials and can be more easily modeled. The underlying continua are assumed to be due to amorphous carbon grains, with the optical properties (type AC2) from Rouleau & Martin (1991). On top of the AC2 grain opacity have been added the two, or in some cases three, additional broad features. The opacity function of the 21 μm feature, with a peak wavelength of 20.1 μm, is derived from the *ISO* SWS06 data (VKH99). The 30 μm feature is modeled by two separate features. For the main feature (which we will continue to call the 30 μm feature), an asymmetrical Gaussian has been used, with a peak wavelength of 27.2 μm and different σ values for the long and short wavelength sides of the peak. This value of the peak wavelength is based upon fits to the infrared spectra of extreme carbon stars (Volk, Xiong, & Kwok 2000). The σ_1 value for the short wavelength side was fixed at 3.6 μm while on the long wavelength side σ_2 was varied to produce the best possible fit. For comparison, the σ_2 value for the long wavelength side was 10.0 μm in the three brightest 21 μm sources, IRAS 07134+1005, 20000+3239, and Z02229+6208, whereas the σ_2 values for the five extreme carbon stars similarly modeled by Volk et al. (2000) ranged from 7.6 to 12 μm. In addition, a 26 μm feature was added using a Gaussian function centered at 25.5 μm with a σ of 2.5 μm. We note at the outset that this fitting of the two features, 30 μm and 26 μm, is not unique. The above method is based on our fitting of the 30 μm feature in five carbon stars, where the 26 μm feature was weak or absent. In these, a good fit was achieved by fitting the 30 μm feature as described above. Then the 26 μm feature was added to this. As mentioned below in the discussion of IRAS Z02229+6208, had we started by first fitting the 26 μm feature, we would get somewhat different peak wavelengths and feature widths, in addition to different relative feature strengths. However, the total amount of relative infrared flux carried by these two features would not be expected to change.

Each dust envelope is assumed to be heated by a central star with a blackbody spectrum of temperature appropriate for its spectral type. In addition to circumstellar extinction, the observations also suffer from interstellar extinction. Approximate values for these are derived from the studies of Neckel & Klare (1980) and Burnstein & Heiles (1982) and are important only for dereddening the short wavelength (visible and near-infrared) photometry, which has been added to extend the SED. The adopted A_V values were obtained by assuming distances of greater than 1 kpc and are listed in Table 1. The following parameters were then adjusted until a good fit was obtained:

1. the power-law index (α) of the density function $\rho_d \propto r^{-\alpha}$;

2. the optical depth of the dust shell at a reference wavelength of 11.22 μm, τ_0;

TABLE 6

RESULTS OF MODEL FITS TO THE SPECTRAL ENERGY DISTRIBUTIONS

	MODEL PARAMETERS							DERIVED PARAMETERS			
					FEATURE STRENGTH						
OBJECT	τ_0 (11.22 μ m)	α	T_* (K)	T_d (K)	30 μm	26 μm	21 μm	L_*/D^2 ($L_\odot$ kpc^{-2})	$\dot{M}/V/D$ $\left(\frac{M_\odot\ \mathrm{yr}^{-1}}{\mathrm{km\ s^{-1}\ kpc^{-1}}}\right)$	r_{in}/D (10^{-3} pc kpc^{-1})	τ_{dyn}/D (yr kpc^{-1})
01005+7910.....	0.0025	3.0	26000	159	0.9	0	0	610	1.0×10^{-8}	4.5	300
02229+6208.....	0.021	2.5	5500	210	1.1	0.7	0.24	1700	1.3×10^{-6}	3.4	220
07134+1005.....	0.007	2.5	7000	165	0.6	0	1.3	1400	7.2×10^{-7}	5.9	540
16594−4656.....	0.04	2.5	8000	173	0.8	0.6	0.9	1500	3.9×10^{-6}	5.5	330
19477+2401.....	0.09	2.5	5500	169	1.1	0.4	0.3	200	2.5×10^{-6}	2.0	130
20000+3239.....	0.013	2.5	5500	171	1.1	0	0.24	630	5.1×10^{-7}	3.4	280
22574+6609.....	0.1	2.0	5500	220	1.5	0.3	0.4	140	3.2×10^{-7}	0.86	32

3. the dust temperature (T_d) at the inner radius (r_{in});
4. the strengths of the 30 (27.2), 26 (25.5), and 21 (20.1) μm features in ratio to the original AC2 opacity function, as needed; and
5. the σ values for the 30 and 26 μm features.

The σ values of the features were changed only as a last resort. The long wavelength σ_2 value for the 30 μm feature had the value of 10.0 in all of the sources except one. For the four sources in which the 26 μm feature was modeled, it was fit with $\sigma = 2.5$ in the two stronger ones and $\sigma = 2.0$ in the two weaker ones. An attempt was made to keep the same 21 μm feature strength as deduced in VKH99; for IRAS Z02229+6208 this did not prove possible.

The models indicated that the dust emission from these objects is optically thin throughout the infrared. In such a case the τ_0 value could be determined only from the amount of extinction suffered by the photospheric continuum by comparing the model to the stellar photometry. Given the unrealistic assumption of a blackbody for the stellar spectrum, and the difficulty in distinguishing between the effects of circumstellar and interstellar extinction, the derived τ_0 values are uncertain to as much as a factor of 2, with corresponding errors in the derived mass-loss rates.

After the spectral shape has been successfully fitted by the model, the model curve is scaled to fit the observed flux. The model parameters are listed in Table 6; also listed are the derived parameters, scaled by the distance D. In order to derive the mass loss rate at the time of shell detachment, a gas-to-dust mass ratio of 330 was assumed. There is an additional uncertainty in these models since the plateau features are not included in the model spectrum. This means that the r_{in} value is probably slightly overestimated, and therefore the parameterized mass loss rate $\dot{M}/V/D$ values are also proportionally overestimated. It appears that this effect is not large since the plateau emission carries only a few percent of the total infrared emission. The uncertainty in τ_0 from the match to the V magnitude is much larger than this. The dynamical age τ_{dyn}/D is derived from r_{in} and the observed expansion velocity of the molecular envelope (Table 1), with the assumption that the velocity of the dust equals that of the gas. For IRAS 01005+7910, we have assumed a typical value of $V_{exp} = 15$ km s^{-1}. A value of $\alpha > 2$ implies that the mass loss rate was increasing with time up to the detachment of the envelope. As a check on these models, we compared our calculated values of the inner radii with the mid-infrared images of the five sources that have been observed (Meixner et al. 1997, 1999). Three of the sources are resolved and two are not; our model values are consistent with the observations in each case.

In Figure 7, the observed spectra and the derived model fits are compared. The spectrum of IRAS 05341+0852 is of such low signal-to-noise ratio that we decided not to model it. From these models we have recalculated the spectrum with normal AC2 grains and with only one of the features present, using the same temperature profile as in the full model. This provides an estimate of the underlying continuum level and of the emission in each individual feature. From the models with and without the features their total fluxes were calculated. The estimated fractions of total flux emitted in the features are listed in Table 7. The total contributions of the plateau features were calculated by subtracting the assumed AC2 continuum from the SWS01 spectrum over the 6–18 μm range. This latter value is somewhat uncertain for IRAS 20000+3239, since the model continuum level does not match the spectrum well around the plateau features. The values were then normalized using the total infrared fluxes for the sources for wavelengths $\lambda > 5$ μm. There is some contribution to the total infrared flux for $\lambda > 45$ μm, which was estimated from the *IRAS* photometry at 60 and 100 μm along with the shape of the model spectra at $\lambda > 100$ μm.

4.1. *Comments on Individual Model Fits*

07134+1005.—A strong 21 μm feature and a 30 μm feature are fitted above the underlying AC continuum. The observed spectrum for IRAS 07134+1005 is somewhat uncertain in band 4 (30 to 45 μm), so we do not ascribe any significance to the slight mismatch between the model and the data in band 4. The model matches the *IRAS* fluxes at 12, 25, 60, 100 μm to within their uncertainties. The visible and near-infrared photometry is taken from Hrivnak, Kwok, & Volk (1989). In this case a reasonably good match

TABLE 7

PERCENTAGE OF TOTAL INFRARED FLUX EMITTED IN THE FEATURES

Object	30 μm	26 μm	21 μm	Plateau
01005+7910.....	18	0	0	15
02229+6208.....	15	5	1	7
07134+1005.....	12	0	8	8
16594−4656.....	16	6	7	8
19477+2401.....	20	3	2	0
20000+3239.....	19	0	1	10
22574+6609.....	18	1	2	11

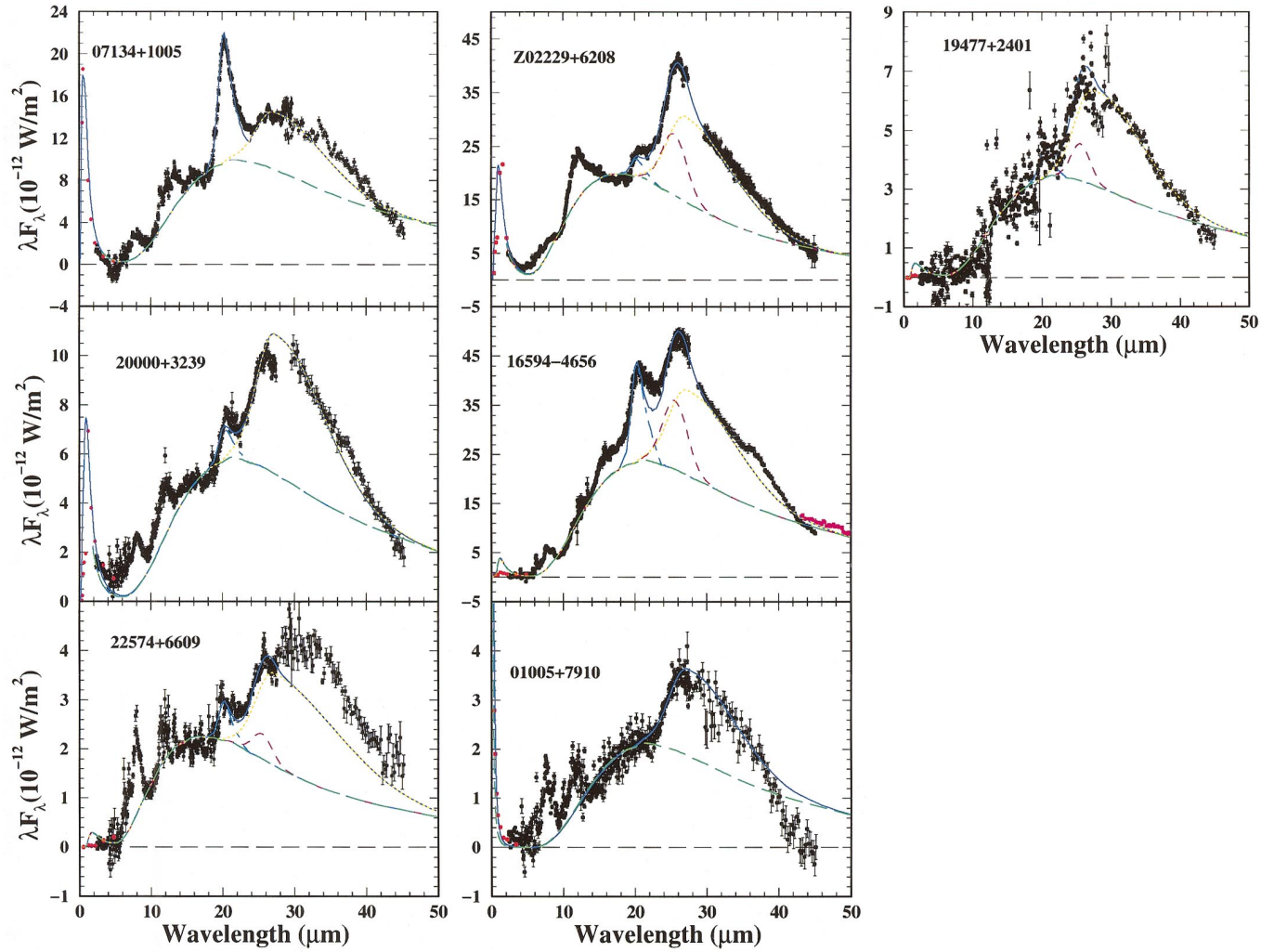

FIG. 7.—Model spectra fitted to the SEDs, showing the overall model fit (*blue solid line*), and the contributions from the amorphous carbon continuum (*green long-dashed line*), the "21 μm" feature (*light blue dashed line*), the "26 μm" feature (*purple short-dashed line*), and the "30 μm" feature (*orange dotted line*). The LWS01 data (for IRAS 16594−4656) are shown as red dots. The *ISO* flux densities for IRAS 01005+7910 and 19477+2401 have been scaled as discussed in the text, and the poor quality data of band 3E (27.5–29.0 μm) have been removed for three of the objects. The short wavelength photometry has been corrected for interstellar extinction.

to the shape of the stellar continuum was obtained. The underlying continua at 5 μm, 10 μm, and 18 μm are also well fitted by the model, with deviations well within 5%. The two plateau features at 8 and 12 μm can clearly be seen above the AC continuum. The 21 μm feature shape in the model matches the peak of the observed spectrum well but falls a bit below the spectrum in the wings, especially on the long wavelength side. It is possible that there is a slight discrepancy in the shape of the 30 μm feature on the short wavelength side that causes this difference between the model and the observations. Or perhaps (more likely) the long wavelength end of the plateau still contains significant flux at 18 μm, and thus the continuum at the short wavelength end of the 21 μm feature has been set too high in the model. The 30 μm feature is relatively weaker in IRAS 07134+1005 than in any of the other sources. There is no sign of the broad 26 μm feature.

20000+3239.—The model fitting to IRAS 20000+3239 was more difficult than for most of the other objects, particularly in the near-infrared wavelength range. A reasonably good fit is obtained with the 30 μm feature and without a 26 μm feature, although inspection of the spectrum does show a local peak at 26.3 μm. We could likely fit the spectrum in this region by some combination of the two features. The 21 μm feature is also well fitted by the model. The fit to the continuum shape between 16 and 18 μm is not as good as in the other sources. The model continuum falls below the data at 10 μm and 7 μm, where a reasonably good match was obtained for the other sources. This suggests that the value used for the dust temperature at the inner radius is too low, but raising this value makes the problem with the continuum near 17 μm much worse. The plotted model spectrum is therefore a compromise between trying to be near the observed continuum at 17 μm as well as not too far below the continuum points at shorter wavelengths. The observed visible and near-infrared photometry is from KHG95. The model τ_0 value was chosen to approximately match the *JHK* flux densities. The visible photometry points are only slightly lower than the model values.

Z02229+6208.—The model matches the continuum at 9 μm and at 17 μm and nicely shows the plateau from 9 to 17 μm and the second broad feature from 7 to 9 μm. An unusual feature of this object is the strong 26 μm feature, which rises far above the other features. It can be fitted by a

Gaussian profile at 25.5 μm with a half-width of 2.5 μm. Had we started the fitting of the spectrum of IRAS Z02229+6208 without the experience of first fitting the 30 μm feature in several extreme carbon stars (Volk et al. 2000) or in IRAS 07134+1005 and 20000+3239, we might have proceeded somewhat differently. We might have centered the 26 μm feature at 26 μm (rather than 25.5 μm) and made it stronger. This would also appear to be a reasonable approach to fitting the spectra of a few of the following objects that we have modeled. However, then the fit to the above objects would require some additional feature and could not simply be fitted by the 30 μm feature. Thus, while our adopted approach to fitting the 26 μm and 30 μm features separately is not unique, we have gone about it in a consistent manner and are confident that it gives a good representation of the combined 26 μm and 30 μm feature strengths. We note that the 26 μm feature has recently also been found in two (of five) extreme carbon stars observed by *ISO* (Volk et al. 2000). However, the feature is found to be wider and stronger in IRAS Z02229+6208 than in the extreme carbon stars ($\sigma = 2.5$ μm compared to $\sigma = 1.5$ μm).

The 21 μm feature strength for this object is found to be larger than the value deduced from the SWS06 observations by VKH99. Since there is only limited continuum baseline available on the long-wavelength side of the 21 μm feature in the SWS06 observations, the uncertainties in the continuum fitting could lead to errors in the derived feature strengths. We do find, however, that good agreement exists for the other objects. The 30 μm feature gives a good fit to the band 4 data. The model fit deviates some from the observations in the near-infrared (4–8 μm). This could be attributed to a variety of reasons: the star not having a blackbody spectrum, a non–spherically symmetric envelope, errors in the scattering parts of the opacity function, etc. The fit in the visible and near-infrared is satisfactory; the observed data are by Hrivnak & Kwok (1999). Even with an α value of 2.5, the model gives too large a flux density at 60 μm. The simulated *IRAS* 60 μm flux density is 83 Jy versus 30.6 Jy observed, including color correction effects. The only way to achieve a better match would be to use an extremely high α value. It is more likely that the dust shell is asymmetric and cannot be described by a simple power law in the outer regions. While such a model could be made, observations do not currently exist to constrain it properly.

19477+2401.—Since the stellar temperature is unknown, the same value was used as for IRAS 20000+3239. These two objects have similarly shaped SWS01 spectra (and also similarly shaped LRS spectra, as noted by Loup et al. 1990), and the data can be fitted by similar models, with two exceptions. A 26 μm feature ($\sigma = 2.0$) was needed for IRAS 19477+2401 and a larger τ_0(11.22 μm) value was used because this object is very faint ($V = 22$) in the visible. The broadband photometric data are from our unpublished observations. The object is known to show a small elliptical nebula (Hrivnak et al. 1999b) and probably possesses additional circumstellar extinction in the visible beyond what is modeled here, which is responsible for the poor fit in the visible wavelengths. A weak 21 μm feature was added to the model, although the spectrum is sufficiently noisy that the existence of this feature is tentative. The model fits well the peak of the spectrum and the continuum shape out to 40 μm and matches the *IRAS* 60 μm flux density within its uncertainty.

22574+6609.—This source is even fainter than IRAS 19477+2401, but it clearly shows the 21 μm, 26 μm, and 30 μm features and the associated strong plateau features. The band 4 spectrum is very uncertain for this source because it was affected by many strong glitches, and although we display these data we have little confidence in their precise values or the error bars displayed. It turned out to be impossible to match the band 4 shape with any reasonable model. We have therefore chosen to concentrate on fitting bands 1–3, along with the *IRAS* 60 and 100 μm flux density values.

A satisfactory model fit was found for a constant mass-loss rate ($\alpha = 2$). The optical depth value is uncertain because the dust envelope is optically thin and the stellar properties are not known. Since the spectral type is not known for this faint ($V = 24$) object, we have assumed the stellar temperature to be 5500 K, the same as for IRAS 20000+3239 and Z02229+6208. The τ_0 value was chosen to produce an approximate match to the L magnitude. The visible and near-infrared photometry is by Hrivnak & Kwok (1991). The model does not match the observations in the visible band. *Hubble Space Telescope* observations show that the object possess a bipolar nebula, with a dark lane obscuring the central star in visible light (Ueta, Meixner, & Bobrowsky 2000). Thus there is a large amount of additional visible extinction present beyond what has been included in our model. This model has a very large value σ_2 value of 14 μm for the 30 μm feature but is still barely able to match the flux density of the very end of band 4. If the typical σ_2 value of 10 μm had been used instead, the match for $\lambda > 30$ μm would have been even poorer. It is not possible to match the SWS01 shape in band 4 without adding in another feature at about 33 μm. Given the uncertainty of the SWS01 spectrum in band 4 for this source, we have chosen not to place much weight on that part of the spectrum.

The amorphous carbon grains produce a good fit to the continuum all the way down to 10 μm, so while there are individual UIR features in the spectrum, there is no extended plateau between 10 and 17 μm. The total observed infrared flux is the smallest of all sources in our sample (see Table 6). If it has a similar intrinsic luminosity to the other sources, then it must be much farther away. This source also has a relatively large expansion velocity for the circumstellar shell ($V_{\rm exp} = 26$ km s^{-1}), leading to a relatively small dynamical age and a very high derived mass-loss rate for the assumed optical depth. This source has a warmer circumstellar shell ($T_d = 220$ K) than any of the other objects, which is consistent with it having a relatively young dynamical age. It is interesting to note that it clearly has the 26 μm feature as does IRAS Z02229+6208, the other source with a higher T_d value. The 21 μm feature strength is somewhat larger than one would deduce from its SWS06 spectrum, which, as with IRAS Z02229+6208, appears to be due to the effect of the 26 μm feature on the underlying continuum. The value of $\sigma = 2.0$ for this 26 μm feature is smaller in IRAS 22574+6609 than in IRAS Z02229+6208, while in both cases it is wider than in models of extreme carbon stars.

01005+7910.—Because of its earlier spectral type (OBe), a much higher stellar temperature ($T_* = 26{,}000$ K) was used than in the other cases. A good fit to most of the spectrum was obtained by simply using an amorphous carbon continuum and a normal 30 μm feature, but no 21 or 26 μm

features. However the best-fit model requires that $\alpha = 3$, and, while it agrees well with the *IRAS* 60 μm flux density, it is 50% too high at 100 μm. The source appears to not have the plateau from 12 to 19 μm seen in the previously discussed sources. The model comes close to fitting the continuum at 10 and 5 μm, and then passes through the V data point. The visible and near-infrared photometry is from our unpublished observations.

18576+0341 and 19306+1409.—These two objects cannot be fitted by our dust radiative-transfer model with the assumption that the underlying continua are due to amorphous carbon grains. It appears that to fit them requires additional heating beyond what can be provided by a single central star. It is possible that these two objects are H II regions or PNs. Another possibility is that the dust is composed of silicate grains, with the UIR features emitted by PAHs that reside closer to the star. Several objects like this have been observed with *ISO* (e.g., CPD $-56°8032$; Cohen et al. 1999). However, we have not tried to model the spectra using silicates.

16594−4656.—We have also modeled the carbon-rich PPN IRAS 16594−4656 (the Water Lily Nebula; Hrivnak, Kwok, & Su 1999a). This object was observed with *ISO* as part of the guest observer program (PGARCIA.PNE). Although IRAS 16594−4656 has a good quality *IRAS* LRS spectrum, it was classified as having silicate absorption on a low-temperature continuum both in the original LRS classification (Atlas of Low-Resolution IRAS Spectra; Olnon et al. 1986) and from independent visual examination of the LRS spectrum (Volk & Cohen 1989). However, we later noted the existence of the 21 μm feature in the LRS spectrum (Hrivnak et al. 1999a), and this is confirmed by *ISO* observations, which show that the 21 μm feature is very strong (Garcia-Lario et al. 1999). The SWS01 spectrum also shows the 3.3, 6.2 and 7.6 μm UIR features, leaving no doubt that the dust shell is carbon rich. One reason for the initial misclassification of the LRS spectrum was the lack of the plateau feature starting at 11 μm, which is our main way to distinguish silicate absorption sources from UIR sources. It should be stressed that the lack of the plateau between 11 and 13 μm in the spectrum of IRAS 16594−4656 is very unusual for either 21 μm sources or objects with UIR features.

ISO Long Wavelength Spectrometer (LWS) data from 43 to 196 μm in mode LWS01 is available for this source, in addition to SWS01 data. We extracted the SWS01 and LWS01 observations from the *ISO* Data Archive, and carried out a normal reduction in ISAP. Garcia-Lario et al. (1999) present a more careful data reduction with special attention to the UIR features, which we did not attempt to duplicate. Our main interest is in the broad dust features and the continuum shape. The central star is clearly visible at the center of a bipolar reflection nebula in the *Hubble Space Telescope* image of IRAS 16594−4656 (Hrivnak et al. 1999a). The optical spectrum presented by Garcia-Lario et al. (1999) shows Hα and Hβ emission lines on a highly reddened spectrum of undetermined spectral type. Lacking more precise information, we have assumed a temperature of 8000 K for the central star.

The model fits well between 24 and 100 μm, then falls somewhat below the LWS01 data at longer wavelengths. However the LWS01 spectrum is not consistent with the *IRAS* photometry at 100 μm—it is more than a factor of 2 brighter—while the model is consistent with the *IRAS* 100 μm point within its uncertainties. It is likely that the excess emission measured in the *ISO* LWS01 spectrum at 100 μm is due to emission from the ISM; no attempt has been made to correct the spectrum for this. There appears to be a plateau feature from 13 to 19.5 μm similar to what is seen in the other 21 μm sources from 15 μm on, but the short wavelength end of the plateau is quite abnormal compared to those of the other objects. The model continuum fits the spectrum at 10 μm and is approximately correct down to 5 μm, excluding the UIR features. Below 5 μm, the fit is not as good. Probably this is due to additional circumstellar extinction caused by a partially obscuring disk, which is not included in the model. The photometric measurements are from van der Veen, Habing, & Geballe (1989) and Hrivnak et al. (1999a).

This object has a strong 21 μm feature, and also a strong 26 μm feature similar to that found in IRAS Z02229+6208. The 30 μm feature is only average in its properties. A σ value of 2.5 μm was derived for the 26 μm feature and a σ_2 value of 10.0 μm was found for the 30 μm feature. Both are typical values. The model − data discrepancy on the long wavelength side of the 21 μm feature is similar that seen for IRAS 07134+1005 but is more pronounced. It appears that this is due to the broad underlying plateau, which is not taken into account in our opacity functions of the features. The dynamical age is calculated using a value of $V_{\rm exp} = 16$ km s^{-1} (Loup et al. 1990).

5. DISCUSSION

Eight of the objects in this paper (excluding 18576+0341 and 19306+1409, but including IRAS 16594−4656, which has been included in the modeling) satisfy the observational properties of PPNs as defined by Kwok (1993) and are almost certainly objects in the post-AGB phase of evolution. They each have a double-peaked SED, consistent with a detached dust shell. For most of them, millimeter-wave observations have revealed molecular emission (CO, HCN) from the expanding remnants of the AGB circumstellar envelopes. The dynamical ages calculated from the models above are several hundred to 1000–2000 yr, based upon assumed distances of one to several kpc. These are in agreement with the ages expected from evolutionary models (Schönberner & Blöcker 1993). Of course, all have mid-infrared emissions from their circumstellar dust, which are seen in the *ISO* spectra we have presented. For the objects that have photospheric spectral types determined by optical spectroscopy, all but one are F or G stars with luminosity class I or Ia. Two additional objects have infrared spectra with a different shape from the others and are likely to be H II regions or young PNs.

The carbon-rich chemistry of several of these was initially indicated by Hrivnak (1995) and Hrivnak & Kwok (1999), who found molecular carbon in absorption in the visible spectra of 10 PPNs with 21 μm emission, including four in this present study. Bakker et al. (1996, 1997) showed from high-resolution visible spectra that the C_2 and CN molecules are located in the CSEs. Omont et al. (1993) found from the ratio of HCN to CO millimeter-wave emission strengths that the envelopes of several of these are carbon-rich. Recent abundance studies based upon high-resolution visible spectra have directly confirmed the high carbon abundances in the photospheres of several of these objects. Studies of IRAS 07134+1005 (Klochkova 1995; Hrivnak et al. 2000, in preparation), 05341+0852 (Reddy et al. 1997),

and Z02229+6208 (Reddy, Bakker, & Hrivnak 1999) show that they are all carbon rich, with [C/Fe] = 0.8–1.2. These studies also show that the objects are metal poor ([Fe/H] = −0.5 to −1.2) and overabundant in *s*-process elements ([*s*-process/Fe] = 1.4–2.0). These abundance values are direct evidence that these three objects are in the post-AGB phase of their evolution.

The UIR features at 3.3, 6.2, 7.7, and 11.3 μm (but not 8.6 μm), commonly seen in H II regions, reflection nebulae, and PNs, are detected in these PPNs. However, *the strengths of these features are relatively weak in PPNs compared to their typical strengths in PNs.* In addition, features are seen at 6.9 and 12.1 μm, and in IRAS 07134+1005 and 22574+6609, a feature at 13.3 μm, and in IRAS Z02229+6208 and 05341+0852, a feature at 14.3 μm.

With the better *ISO* spectral resolution, one can resolve the major 7.7 μm C—C stretching band. This feature has been difficult to observe in the past because it is at the edge of an atmospheric window. Based on their KAO observations of two 21 μm sources (IRAS 07134+1005 and 22272+5435), Buss et al. (1990) have noted that, in comparison to PNs and H II regions, the 7.7 μm feature in these is weak compared to the strong 8 μm plateau, the 11.3 μm feature is weak compared to the broad 12 μm plateau, and the 6.9 μm feature is strong compared to the 6.2 μm feature. The same general relationships are found in the spectra of three of our objects: IRAS Z02229+6208, 07134+1005, and 20000+3239 (except the 6.9-to-6.2 μm ratio). For IRAS 22574+6609, the feature at 7.7 μm is relatively stronger than in the three sources above but still sits on an 8 μm plateau. For IRAS 05341+0852, the feature at 11.3 μm is relatively stronger than in the three above but still clearly lies on a 12 μm plateau (as is seen more clearly in the CGS3 spectrum in KHG95). For IRAS 19477+2401, the UIR emission features are not seen, but a weak 12 μm plateau and the 26 and 30 μm features appear to be present. It is on the basis of this similar general shape of the mid-infrared emission to that of the above five objects, plus the detection of HCN, that we conclude that IRAS 19477+2401 possesses a carbon-rich chemistry.

IRAS 01005+7910, 18576+0341, and 19306+1409 are different. For IRAS 01005+7910, the 7.7 μm feature is much stronger than the 8 μm plateau and there is no 12 μm plateau. The features at 6.2, 8.6, and 11.3 μm are all strong. Its infrared spectrum in this region is more similar to the young carbon-rich PN IRAS 21282+5050, which has been observed by *ISO* (Beintema et al. 1996; Molster et al. 1996).[3] IRAS 01005+7910 has a spectral classification as an OB emission star, which is much hotter than the others listed above. Thus for IRAS 01005+7910 one is probably seeing the affect of the evolution in temperature of the central star on the excitation of the UIR features. For IRAS 18576+0341, the 6.2 μm feature is very strong compared to 6.9 μm and the 7.7 μm feature is very strong on a weak 8 μm plateau, and the 11.3 μm feature is strong on a sharply rising continuum. Since no central star is visible for this object, it may be that it is actually not a PPN but rather an obscured H II region. Its spectrum in the region 6–12 μm looks similar to the spectra of compact H II regions observed with *ISO* (Roelfsema et al. 1996). IRAS 19306+1409 also lacks a 12 μm plateau and possesses features at 6.2 and 7.7 μm. It possesses a visible star, and based on a recent near-infrared spectrum we suspect that it is a young PN.

The only other published complete *ISO* SWS spectrum of a PPN is that of the object IRAS 16594−4656, which also has a 21 μm feature. Garcia-Lario et al. (1999) list emission features at 3.3, 6.2, 7.7, 8.6, 11.3, 12.6, and 13.4 μm. The *ISO* spectrum of IRAS 16594−4656 is displayed in Figure 7. It also shows the strong 26 μm feature, peaking at 26.0 μm. In its general feature ratios in the region 3–12 μm, it is most similar to IRAS 01005+7910. It is also a carbon-rich object with Hα and Hβ emission, but the spectral type is unknown. Perhaps it also shows the effects of evolution on its UIR features as compared with the cooler central stars of most of the PPNs in this study.

Thus in the objects with hotter central stars (IRAS 01005+7910, 16594−4656, presumably 18576+0341 and 19306+1409), the 7.7 and 11.3 μm features appear stronger, more similar to those observed in PNs. The changing ratios of the 6.9, 12.2, and 13.3 μm to the 7.7 and 11.3 μm features suggest a reduction in the H/C ratio as a star evolves from the PPN to the PN phase (Guillois et al. 1996).

In Figure 8, are shown the relative strengths of the emission features and plateaus to the underlying AC continuum. This figure supports the results of Table 6 (feature strengths) and Table 7 and allows one to see in graphical form the strengths of the features in each source and to look for correlations. Below 10 μm the continuum fitting is generally not as good, and thus these feature strengths are less accurate. The spectrum of IRAS 19477+2401 is very noisy over most of its spectral range. The relative strengths of the features at longer wavelengths can be seen in Figure 7.

We have found a new feature at "26 μm" in the spectra of eight of these sources, including IRAS 16594−4656. It is perhaps not surprising that it has not been detected prior to *ISO*. There has not been much spectroscopic work at this wavelength, which is beyond the long wavelength end of the *IRAS* LRS spectra. At lower resolution it blends with the "30 μm" feature. There may be some evidence for it in the published KAO data. O95 note an emission feature at this wavelength in the carbon-rich PPN IRAS 23304+6147 but state that it may not be real but rather due to a notch in the order-sorting filter appearing in that channel. However, it may also be present in other of their sources as well. Szczerba et al. (1999), using *ISO* SWS06 spectra of two additional carbon-rich PPNs, first point out this substructure in the 30 μm feature; they call attention to a "plateau" that extends from 26 to 27 μm. This is indeed the 26 μm feature, which is seen more clearly in our larger sample. Volk et al. (2000) also find the feature to be present in two of the five extreme carbon stars they studied with *ISO*. The pre-*ISO* mid-infrared spectrum of the young, carbon-rich PN IC 418 presented by Cox (1993) seems to show a feature at 26 μm, in addition to the 30 μm feature. Thus there appears to be evidence for the presence of the 26 μm feature in previous spectra, but it is displayed clearly here for the first time.

There have been several suggestions as to the origin of the 21 μm feature, ranging from various carbon-based species to SiS_2. We will not review these here; a recent summary can be found in Kwok et al. (1999). However, the

[3] The *ISO* spectrum of IRAS 01005+7910 is also similar to that of HR 4049 (Beintema et al. 1996; Molster et al. 1996), a binary system with a strong infrared excesses presumably arising from a circumbinary disk (Van Winckel 1999). This object is undergoing a different evolution that the PPNs considered here.

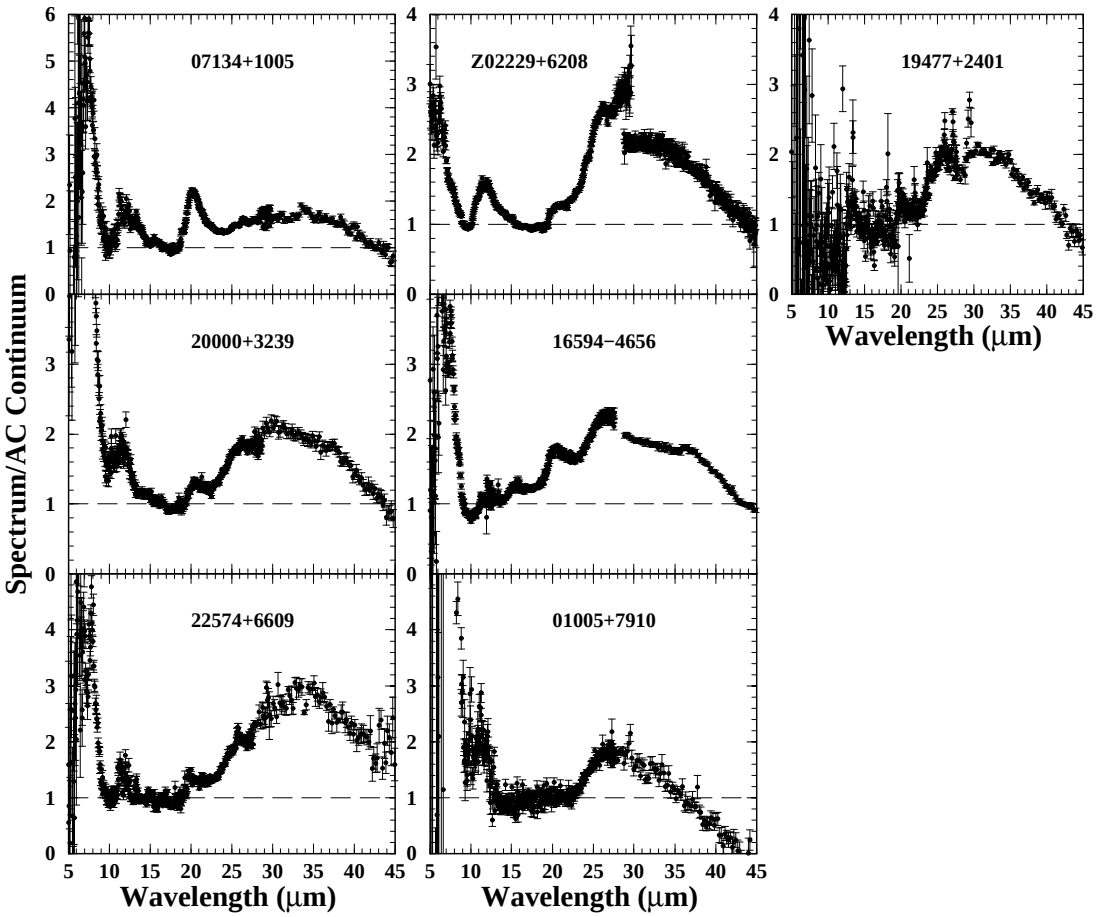

FIG. 8.—Relative strengths of the spectral features with respect to the underlying amorphous carbon continuum. IRAS 19477+2401 is extremely noisy below 13 μm, as discussed in the text. (Note that the poor-quality band 3E data have been removed from the spectrum of IRAS 16594−4656, but not from Z02229+6208 and 20000+3239 as they had been in Fig. 7.)

absence of the predicted companion feature at 16.5 or 17 μm appears to rule out SiS_2 (Begemann et al. 1996; Kraus, Nunth, & Nelson 1997). The origin of the 30 μm feature is also uncertain, although there have been several suggestions, such as MgS (Goebel & Moseley 1985; see also the recent discussion by Szczerba et al. 1999). The resolution of the 30 μm feature into separate features at 27.2 and 25.5 μm should aid in its identification.

6. CONCLUSIONS

It is clear from our observations that the infrared emission features seen in carbon-rich PPNs are different from those observed in carbon-rich PNs or reflection nebulae in the ISM. The UIR features at 3.3, 6.2, 7.7, and 11.3 μm due to various aromatic vibrational modes are not as strong as their counterparts in PNs. In contrast, the aliphatic band at 6.9 μm, never seen in PN, is detected in IRAS Z02229+6208, 05341+0852, 07134+1005, 20000+3239, and 22574+6609. Also prominent in the PPN spectra are the broad plateaus observed around 8 and 12 μm.

Five, and possibly seven, of the 10 objects (including IRAS 16594−4656) show the 21 μm and 30 μm emission features. Two of the 30 μm detections confirmed earlier observations; the rest are new, and taken together with the five sources observed by Omont et al. (1995), suggest that all of the 21 μm sources also possess the 30 μm feature. However, as stated earlier, the 30 μm feature is seen in a broader range of carbon-rich objects, from AGB stars to PNs. The 30 μm feature has been resolved into a feature at 27.2 μm (which we call the "30 μm" feature) and a new feature at 25.5 μm (the "26 μm" feature). The 21 μm feature is strongest in IRAS 07134+1005 (8% of total infrared flux emitted) and then IRAS 16594−4656 (7%), and weaker in the other sources (0%–2%). The 30 μm feature (excluding the 26 μm feature), on the other hand, is weaker in the two strong 21 μm sources. In IRAS 07134+1005, the total infrared flux carried in the 30 and 26 μm features combined is 12%, much less than that contained in these two features in the other PPNs (18%–23%).

The new feature at 26 μm is detected in seven objects. This feature appears to be present in a broader range of objects—carbon stars, PPNs, and possibly PNs—than does the 21 μm feature, which has been seen only in PPNs. In this way, the 26 μm feature is similar to the 30 μm feature, and since all of the objects that have been seen thus far to possess the 26 μm feature also possess the 30 μm feature, it may be that the two are closely related. Clearly more observational work is needed to define the characteristics of the 26 μm feature and the conditions in which it is found. In the present study, it is seen to be especially strong in IRAS Z02229+6208 and 16594−4656.

In a previous study, we found that the 21 μm feature has the same characteristic shape in each of the sources in which it has been found and that it has a peak wavelength of 20.1 μm (VKH99). The present results are consistent with this. The 30 μm feature is found to be fitted by an asymmetrical

Gaussian, with a peak wavelength of 27.2 μm and σ values of 3.6 μm on the short-wavelength side and typically 10.0 μm on the long-wavelength side. The new 26 μm feature has a peak wavelength of 25.5 μm and is fitted by a symmetrical Gaussian with σ ranging from 2.5 to 2.0 μm. With the radiative-transfer models, we have also demonstrated that significant amounts of energy (25%–37% in total) are emitted in the 21 μm, 26 μm, 30 μm, and plateau features. These results pose serious constraints on the chemical constituents of the materials responsible for these features, limiting them to elements of high abundance. Our spectra seem to rule out SiS_2. The carbon-rich nature of these PPNs suggests carbon as a natural major ingredient. While the UIR features point to the presence of C—H, C—C, and C=C bonds in various aromatic and aliphatic structures, a comprehensive model of the origin of the UIR features will emerge only when we have a consistent understanding of the chemical interplay between the UIR, 21 μm, 26 μm, 30 μm, and the plateau features.

Thus a consistent picture of chemical evolution beyond the AGB is emerging from the *ISO* observations reported here. The UIR and 30 μm features, widely observed in PNs, are already present in PPNs. They coexist with broad, strong plateau features at 8 and 12 μm, which can be due only to a very large molecule or solid-state material. Even if the UIR features originate from simple (<50 atoms) molecules such as PAHs, the plateau features suggest that chemical processing in the circumstellar environments of these stars are capable of synthesizing very complex molecules over a very short (several hundred years) time. Once these molecules are formed, they also undergo rapid changes in structures, as evidenced by the changing strengths of the UIR features from PPNs to PNs, a transition that is believed to last no more than a few thousand years. This chemical evolution is supported by our observations that PPNs with hotter central stars have UIR feature strengths more similar to those of PNs. These results show that PPNs have an important role to play in our understanding of circumstellar chemistry.

We thank F. Molster for helpful discussions about the *ISO* SWS data, the referee, M. Meixner, for several helpful suggestions, and the staff at IPAC for help with the data reduction. We also thank D. Kester and P. Roelfsema for use of the SRON IRAS data server to extract the LRS spectrum of IRAS 01005+7910, and T. Hasegawa for assistance in the processing of the JCMT data. The JCMT is operated by the Joint Astronomy Centre on behalf of the Particle Physics and Astronomy Research Council of the United Kingdom, the Netherlands Organization for Scientific Research, and the National Research Council of Canada. This work is supported in part by NASA grants to B. J. H. through NASA (NAG5-3346) and through contract 961534 from the Jet Propulsion Laboratory, and in part by grants to S. K. and K. V. from the Natural Science and Engineering Research Council of Canada.

REFERENCES

Allamandola, L. J., Tielens, A. G. G. M., & Barker, J. R. 1989, ApJS, 71, 733
Bakker, E. J., van Dishoeck, E. F., Waters, L. B. F. M., & Schoenmaker, T. 1997, A&A, 323, 469
Bakker, E. J., Waters, L. B., F. M., Lamers, H. J. G. L. M., Trams, N. R., & Vander Wolf, F. L. A. 1996, A&A, 310, 893
Begemann, B., Dorschner, J., Henning, Th., & Mutschke, H. 1996, ApJ, 464, L195
Beintema, D.A. et al. 1996, A&A, 315, L369
Burnstein, D., & Heiles, C. 1982, AJ, 87, 1165
Buss, R. H., Jr., Cohen, M., Tielens, A. G. G. M., Werner, M. W., Bregman, J. D., Witteborn, F. C., Rank, D., & Sandford, S. A. 1990, ApJ, 365, L23
Cohen, M., Barlow, M. J., Sylvester, R. J., Liu, X.-W., Cox, P., Lim, T., Schmitt, B., & Speck, A. K. 1999, ApJ, 513, L135
Cox, P. 1993, in ASP Conf. Ser. 41, Astronomical Infrared Spectroscopy, ed. S. Kwok (San Francisco: ASP), 163
Dayal, A., Hofmann, W. F., Bieging, J. H., Hora, J. L., Deutsch, L. K., & Fazio, G. G. 1998, ApJ, 492, 603
de Graauw, Th. et al. 1996, A&A, 315, L49
Forrest, W. J., Houck, J. R., & McCarthy, J. F. 1981, ApJ, 248, 195
Garcio-Lario, P., Manchado, A., Ulla, A., & Manteiga, M. 1999, ApJ, 519, 941
Geballe T. R., & van der Veen, W. E. C. J. 1990, A&A, 235, L9
Goebel, J., & Moseley, S. 1985, ApJ, 290, L35
Guillois, O., Nenner, I., Papoular, R., & Reynaud, C. 1996, A&A, 464, 810
Hrivnak, B. J. 1995, ApJ, 438, 341
Hrivnak, B. J., & Kwok, S. 1991, ApJ, 368, 564
———. 1999, ApJ, 513, 869
Hrivnak, B. J., Kwok, S., & Geballe, T. R. 1994, ApJ, 420, 783
Hrivnak, B. J., Kwok, S., & Su, K. Y. L. 1999a, ApJ, 524, 849
Hrivnak, B. J., Kwok, S., & Volk, K. M. 1989, ApJ, 346, 265
Hrivnak, B. J., Langill, P. L., Su, K. Y. L., & Kwok, S. 1999b, ApJ, 513, 421
Justtanont, K., Barlow, M. J., Skinner, C. J., Roche, P. F., Aitken, D. K., & Smith, C. H. 1996, A&A, 309, 612
Kessler, M. F., et al. 1996, A&A, 315, L27
Klochkova, V. G. 1995, MNRAS, 272, 710
Kraus, G. F., Nunth, J. A., III, & Nelson, R. N. 1997, A&A, 328, 419
Kwok, S. 1993, ARA&A, 31, 63
Kwok, S., Hrivnak, B. J., & Geballe, T. R. 1990, ApJ, 360, L23
———. 1995, ApJ, 454, 394 (KHG95)
Kwok, S., Volk, K., & Bidelman, W. 1997, ApJS, 112, 557
Kwok, S., Volk, K. M., & Hrivnak, B. J. 1989, ApJ, 345, L51 (KVH89)
———. 1999, in IAU Symp 191, Asymptotic Giant Branch Stars, ed. T. Le Bertre, A. Lebre, & C. Waelkens (San Francisco: ASP), 297
Lemke, D., et al. 1996, A&A, 315, L64
Leung, C. M. 1976, ApJ, 209, 75
Lindqvist, M., Nyman, L.-Å., Olofsson, H., & Winnberg, A. 1988, A&A, 205, L15
Loup, C., Forveille, T., Nyman, L. Å., & Omont, A. 1990, A&A, 227, L29
Meixner, M., Skinner, C. J., Graham, J. R., Keto, E., Jernigan, J. G., & Arens, J. F. 1997, ApJ, 482, 897
Meixner, M., et al. 1999, ApJS, 122, 221
Molster, F. J., et al. 1996, A&A, 315, L373
Neckel, Th., & Klare, G. 1980, A&AS, 42, 251
Olnon, F. M., et al. 1986, A&AS, 65, 607
Omont, A., Loup, C., Forveille, T., te Lintel Hekkert. P., Having, H., & Sivagnanam, P. 1993, A&A, 267, 515
Omont, A., et al. 1995, ApJ, 454, 819 (O95)
Reddy, B. E., Bakker, E. J., & Hrivnak, B. J. 1999, ApJ, 524, 831
Reddy, B. E., Parthasarathy, M., Gonzalez, G., & Bakker, E. J. 1997, A&A, 328, 331
Roelfsema, P. R., et al. 1996, A&A, 315, L289
Rouleau, F., & Martin, P. G. 1991, ApJ, 377, 526
Schaeidt, S. G., et al. 1996, A&A, 315, L55
Schönberner, D., & Blöcker, T. 1993, in ASP Conf. Ser. 45, Luminous High-Latitude Stars, ed. D. D. Sasselov (San Francisco: ASP), 337
Schultz, B., et al. 1999, in The Universe as Seen by *ISO*, ed. P. Cox and M. F. Kessler (Noordwijk: ESA), 89
Szczerba, R., Henning, Th., Volk, K., Kwok, S., & Cox, P. 1999, A&A, 345, L39
Ueta, T., Meixner, M., & Bobrowsky, M. 2000, ApJ, 528, 861
van der Veen, W. E. C. J., Having, H. J., & Gaballe, T. R. 1989, A&A, 226, 108
Vanetijn, E. A., et al. 1996, A&A, 315, L60
Van Winckel, H. 1999, in IAU Symp 191, Asymptotic Giant Branch Stars, ed. T. Le Bertre, A. Lebre, & C. Waelkens (San Francisco: ASP), 465
Volk, K., & Cohen, M. 1989, AJ, 98, 931
Volk, K., Kwok, S., & Hrivnak, B.J. 1999, ApJ, 516, L99 (VKH99)
Volk, K., Xiong, G.-Z., & Kwok, S. 2000, ApJ, 530, 408